Progress in Oceanography 229 (2024) 103322

Contents lists available at ScienceDirect

Progress in Oceanography

journal homepage: www.elsevier.com/locate/pocean

Water mass evolution and general circulation of Baffin Bay: Observations from two shipboard surveys in 2021

Jie Huang [a,*], Robert S. Pickart [a], Frank Bahr [a], Leah T. McRaven [a], Jean-Éric Tremblay [b], Christine Michel [c], Emil Jeansson [d], Ben Kopec [e], Jeffrey M. Welker [f,g,h], Sólveig R. Ólafsdóttir [i]

[a] Woods Hole Oceanographic Institution, Woods Hole, MA 02543, USA
[b] Québec-Océan and Takuvik Joint International Laboratory, Department of Biology, Laval University, Québec City, Québec G1V 0A6, Canada
[c] Fisheries and Oceans Canada, Winnipeg, Manitoba R3T 2N6, Canada
[d] NORCE Norwegian Research Centre, Bjerknes Centre for Climate Research, Bergen 5007, Norway
[e] Great Lakes Research Center, Michigan Technological University, Houghton, MI 49931, USA
[f] University of Oulu, Oulu 90014, Finland
[g] University of Alaska Anchorage, Anchorage, AK 99508, USA
[h] University of the Arctic, Rovaniemi 96200, Finland
[i] Marine and Freshwater Research Institute, Reykjavik IS-220, Iceland

ARTICLE INFO

Keywords:
Arctic Ocean
Baffin Bay
Water Masses
Freshwater
Basin-scale circulation

ABSTRACT

Baffin Bay is an Arctic marginal sea connected to the North Atlantic via Davis Strait and the Labrador Sea. While the exchange of heat and freshwater through Davis Strait is known to strongly influence the subpolar North Atlantic, there are significant gaps in our understanding of the circulation and water mass distribution and transformation throughout Baffin Bay, in part due to limited direct velocity observations. In this study, high-resolution hydrographic, nutrient, oxygen isotope, and velocity data from two shipboard surveys in late-summer to early-fall 2021 are used to address these gaps. During the time period of observation, Baffin Bay was dominated by cold, fresh, nitrate-depleted Polar Water (PW) in the upper 300 m, with the coldest and freshest PW distributed along the western shelf and slope adjacent to Baffin Island. Only a small amount of warm and salty Atlantic-origin water was measured entering the southeastern bay at depth, which is diluted rapidly when passing through Davis Strait. Pacific-origin freshwater was dominant in the upper 200 m on the western side, with relatively small amounts of meteoric water on both sides of the bay. The circulation in Baffin Bay was generally cyclonic, consisting of a strong, surface-intensified western boundary current and a slower, weakly baroclinic eastern boundary current. Much of the eastern boundary current bifurcated to the west at the northern end of the Labrador Sea, and, as the remaining flow progressed through Davis Strait, it transitioned from surface-intensified to bottom-intensified. Basin-scale recirculation of the PW was documented using the shipboard data, which was also evident in the velocity field of an ocean reanalysis product for the same time period. Examination of the reanalysis fields from 1993 to 2021 indicates that the circulation in Baffin Bay was anomalously cyclonic during summer/fall 2021. Such basin-scale circulation anomalies can arise due to both the local wind stress curl pattern and remote wind forcing associated with the Arctic Oscillation index.

1. Introduction

Baffin Bay, located between Greenland and Baffin Island Canada, is a critical marginal sea where the fresh and cold Polar Water (PW) from the Arctic Ocean interacts with the warm and salty Atlantic Water (AW) from the subpolar North Atlantic. Due to the warming climate, the amount of freshwater in the Arctic Ocean has been increasing substantially over the past two decades, associated with melting ice and riverine discharge (Proshutinsky et al., 2009; Solomon et al., 2021). If and when there is a release of this freshwater, there is uncertainty regarding the pathways the water will take, including how it will progress through Baffin Bay. The extent to which this freshwater can subsequently be fluxed into the Labrador Sea and interior subpolar North Atlantic has the potential to impact the North Atlantic meridional

* Corresponding author.
E-mail address: jhuang@whoi.edu (J. Huang).

https://doi.org/10.1016/j.pocean.2024.103322
Received 6 March 2024; Received in revised form 26 July 2024; Accepted 7 August 2024
Available online 9 August 2024

overturning circulation (Lazier, 1980; Böning et al., 2016; Zhang et al., 2021; Lin et al., 2023), which is a critical component of Earth's climate system (Rossby, 1996; Buckley & Marshall, 2016). At the same time, the warm AW advected along the Greenland boundary current system has been implicated in causing basal melt in Greenland's glaciers, both on the east and west coasts (Holland et al., 2008; Straneo et al., 2012; Myers & Ribergaard, 2013; Gladish et al., 2015; Mortensen et al., 2018; Rysgaard et al., 2020). However, detailed measurements are lacking regarding the distribution and transformation of this water as it circulates and interacts with the fresh and cold PW through Baffin Bay.

A schematic of the circulation in the region of Baffin Bay and the northern Labrador Sea is shown in Fig. 1, based on previous observations and modeling. The West Greenland boundary current system that stems from Cape Farewell is the source of water feeding Baffin Bay from the south. It consists of the following components: a coastal current (West Greenland Coastal Current; WGCC) transporting the freshest water (Lin et al., 2018; Gou et al., 2022; Mortensen et al., 2022; Foukal & Pickart, 2023); a shelfbreak jet (West Greenland Current; WGC) carrying the warm and salty subtropical-origin AW beneath the fresh surface layer (Pacini et al., 2020); and a deep component (Deep Western Boundary Current; DWBC) transporting Labrador Sea Water and the dense overflow waters from the Nordic Seas (Pacini et al., 2020). Progressing northward, the WGC experiences two major disruptions. Shortly beyond Cape Desolation (Fig. 1), the current becomes both baroclinically and barotropically unstable due to the steepening continental slope (Katsman et al., 2004; Bracco et al., 2008) and sheds large anticyclonic eddies known as Irminger Rings. These Rings transport freshwater offshore in the surface layer and AW at depth (Lilly et al., 2003; De Jong et al., 2014). A bit farther to the north the WGC bifurcates: part of the current is diverted into the northern Labrador Sea, while the remaining portion remains near the boundary and progresses northward through Davis Strait (Cuny et al., 2002) (Fig. 1). Based on the Davis Strait mooring observations from 2004 to 2010 (Curry et al., 2014), the northward transport of the water stemming from WGC+WGCC is about 1.1 Sv (1 Sv = 10^6 m^3 s^{-1}). North of Davis Strait in Baffin Bay, the transport, evolution, and ultimate fate of the WGC and WGCC remains unclear.

The circulation in Baffin Bay is suggested to be cyclonic. This understanding is based on hydrographic signatures (Zweng & Münchow, 2006; Münchow et al., 2015), sparse mooring records (Tang et al., 2004), and numerical models (Dunlap & Tang, 2006; Dukhovskoy et al., 2016; Zhang et al., 2016). It is believed that the WGC continues northward and largely recirculates south of Nares Strait (Fig. 1), with the AW becoming progressively colder and fresher. The current is subsequently joined by cold, fresh outflows from Nares Strait (via Smith Sound; Münchow, 2016), Jones Sound (Melling et al., 2008), and Lancaster Sound (Peterson et al., 2012) to form the southward-flowing Baffin Island Current (BIC, Tang et al., 2004, Fig. 1). These cold and fresh outflows are suggested to be partly of Pacific origin, originating in Bering Strait and entering Baffin Bay through the Canadian Arctic Archipelago

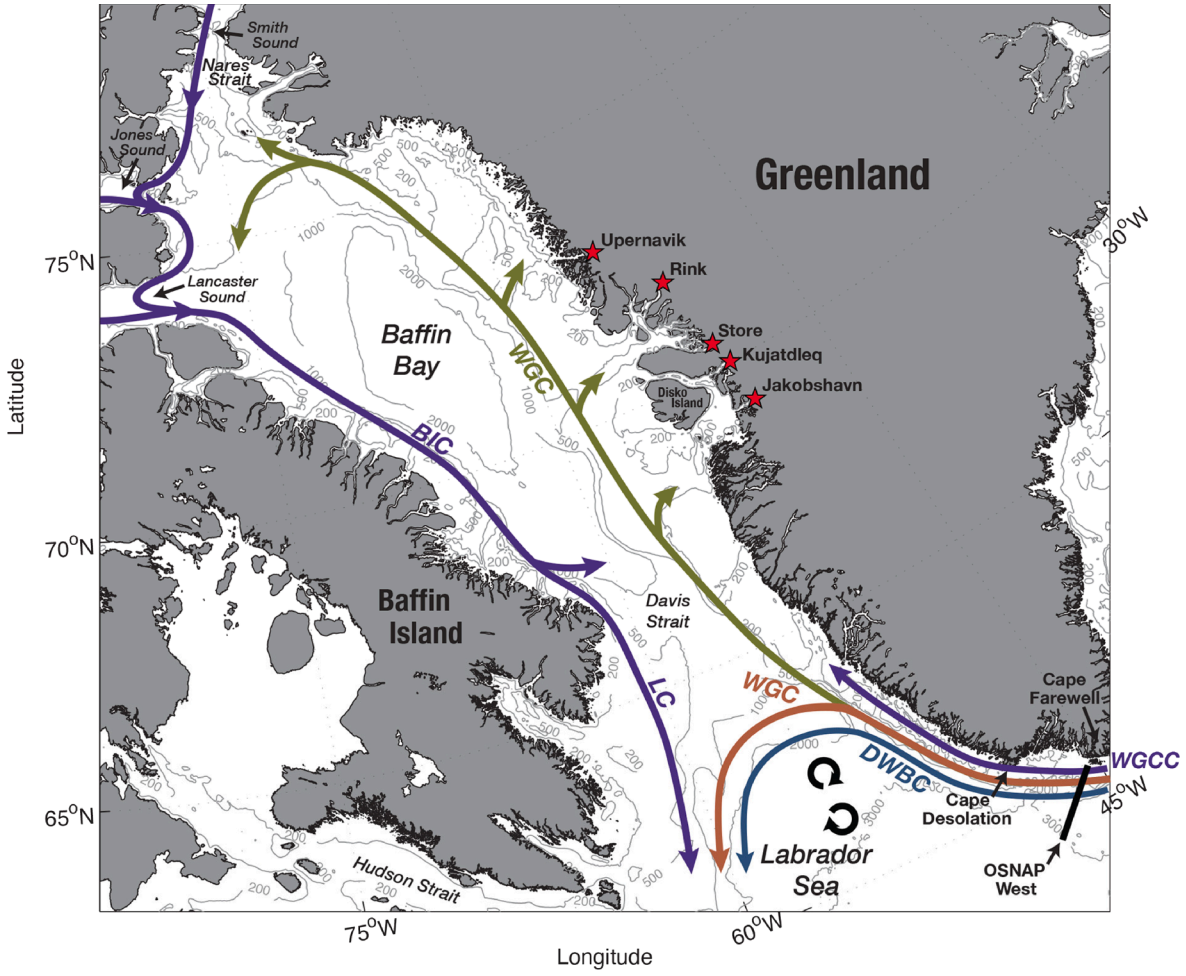

Fig. 1. Schematic circulation in Baffin Bay and the northern Labrador Sea, including place names. The Uummannaq region glaciers are marked by the red stars. The two small anti-cyclones denote Irminger Rings. The Overturning of the Subpolar North Atlantic Program (OSNAP) West section is indicated by the black line. WGC=West Greenland Current; WGCC=West Greenland Coastal Current; BIC=Baffin Island Current; LC=Labrador Current. The bathymetry (gray contours) is from ETOPO1.

(Jones et al., 2003; Azetsu-Scott et al., 2010; 2012). Based on the mooring observations, the net transport across the northern gateways of Baffin Bay is about 1.7 Sv (positive means transport into the bay), including 0.9 ± 0.1 Sv through Nares Strait (Münchow, 2016), 0.3 ± 0.1 Sv through Jones Sound (Melling et al., 2008), and 0.46 ± 0.09 Sv through Lancaster Sound (Peterson et al., 2012). The net transport from the north balances (within measurement uncertainty) that exiting Baffin Bay measured by the mooring array deployed in Davis Strait, −1.6 ± 0.5 Sv (Curry et al., 2014).

In addition to the mean conditions described above, there have been studies investigating the seasonal to long-term changes of water masses in Baffin Bay. For example, using mooring data Tang et al. (2004) suggested that seasonal variations of temperature and salinity in the bay are small, except in Davis Strait, the shelf of the northern Bay, and the mouth of Lancaster Sound. Using an historical hydrographic dataset, Zweng and Münchow (2006) identified significant freshening and warming of the deep basin from the 1910s to the 2000s, the latter likely associated with the warming temperatures of the inflowing AW from the south. Variability of the flow through the northern and southern gateways of Baffin Bay, including possible driving mechanisms, has been investigated as well (Peterson et al., 2012; Myers et al., 2021; Wang et al., 2022). For instance, the southwesterly winds in the Beaufort Sea, which are parallel to the western coasts of the Canadian Arctic Archipelago, were found to be significantly correlated with the transport through Lancaster Sound (Peterson et al., 2012). Also, the net transport through Davis Strait reversed from southward to northward for a month at the end of 2010 due to anomalous southerly wind along the western coast of Greenland (Myers et al., 2021). In addition to the wind forcing, the along-channel pressure gradient was suggested to drive southward flow across Nares Strait during fast ice conditions when there is a higher sea level in the Arctic (Melling et al., 2001; Rabe et al., 2012). Furthermore, a sea level drop in the North Atlantic subpolar gyre was linked to an extreme event of enhanced southward volume transport through Davis Strait in the mid-to-late 2010s (Wang et al., 2022).

While velocity observations are somewhat common at the gateways, there are very few measurements of direct velocity in the interior of Baffin Bay. Münchow et al. (2015) is one of the few examples, but their velocity measurements in the northern and western bay were collected about 20 years ago and rapid changes are taking place in the high latitude ocean due to the warming climate. As such, there has been no quantitative description of the large-scale boundary current structure and transport in Baffin Bay, or a description of the interior circulation from the observational perspective. These limitations have left large uncertainties as to the variability and driving mechanisms of basin-scale circulation in the bay. There are many unanswered questions in this regard. For example, both models (Dukhovskoy et al., 2016) and observations (Münchow et al., 2015) indicate strong lateral exchange between the slope and basin. This likely impacts the structure and transport of the boundary current system encircling Baffin Bay, but this remains undetermined. Despite the dominance of cyclonic flow in Baffin Bay, the model of Tang et al. (2004) indicates a southward-flowing counter current on the Greenland slope that extends from about 72°N towards Davis Strait. In addition, it has been argued that water transported by the BIC can be diverted to the West Greenland shelf and subsequently flow into fjords (Gladish et al., 2015) as well as southward through Davis Strait (Rysgaard et al., 2020). Presently, it is unclear how prevalent such detailed circulation features are.

In this study, we use hydrographic, nutrient, oxygen isotope, and velocity data from two Baffin Bay shipboard surveys conducted from late-summer to early-fall 2021, along with output from ocean reanalysis products (Section 2), to help fill the gaps in our understanding of the general circulation and water mass distribution and evolution in Baffin Bay. The characteristic water masses and their distribution over the broad area of the bay are documented, together with the different water mass sources into the bay identified using nutrient and oxygen isotope data (Sections 3.1 and 3.2). We then characterize the structure of the boundary currents, quantify their volume transport, and document the evolution of the water masses they circulate around the bay based on a collection of high-resolution sections (Sections 3.3 and 3.4). Finally, the variability of the basin-scale circulation, as well as the representativeness of our velocity observations, is investigated using an ocean reanalysis product, including the impact of local and remote wind forcing (Section 3.5).

2. Data and methods

2.1. Shipboard data

The shipboard hydrographic, nutrient, oxygen isotope, and velocity data used in this study were primarily collected on the United States Coast Guard Cutter (USCGC) *Healy* from 17 September to 4 October 2021. The dataset consists of a set of sections covering the boundaries and interior of Baffin Bay (see Fig. 2 for the station locations). Approximately a month prior to the *Healy* cruise, a survey focusing on the regional ecosystem was carried out on the Canadian Coast Guard Ship (CCGS) *Amundsen*. While *Amundsen's* geographical sampling domain was broader than Baffin Bay, as part of their survey they collected hydrographic, nutrient, and velocity data at the northern and southern gateways of Baffin Bay, including sections across the southern part of Nares Strait (hereafter referred to as Nares Strait), Lancaster Sound, and the region north of Davis Strait (Fig. 2). In general, the *Healy* sections had higher spatial resolution than the *Amundsen* sections (5–15 km versus 10–20 km).

2.1.1. Hydrographic data

A Sea-Bird 911 + conductivity-temperature-depth (CTD) rosette system with 24 Niskin bottles for seawater sampling was used on the two surveys. *Healy's* CTD hydrographic data (McRaven, 2022) were processed using Sea-Bird data processing software version 7.22.0. The raw CTD data were converted from HEX to human-readable ASCII format, lag corrected, edited for large spikes, smoothed according to sensor, and pressure averaged into 1 dbar bins for final data quality control and analysis. The temperature and conductivity sensors were calibrated at Sea-Bird prior to and after the field season, and the resulting accuracy is 0.003 °C for temperature and 0.006 for practical salinity (for details see the documentation on the website containing the Healy data, https://arcticdata.io/catalog/view/doi%3A10.18739%2FA2DB7VR5M). *Amundsen's* CTD data (Amundsen Science Data Collection, 2021) were processed by the Québec-Océan and Amundsen Science group, including sensor calibration and data quality control (for details see their data website, https://www.polardata.ca/pdcsearch/?doi_id=12713). The vertical resolution of the final *Amundsen* temperature and salinity profiles is 1 dbar, with similar accuracy for temperature and practical salinity as the *Healy* data. Expendable CTDs (XCTDs, with a maximum measurement depth of 1000 m) were used during the *Healy* survey to broaden the sampling domain and save time. The accuracy of the XCTD measurements is 0.02 °C for temperature and 0.03 for practical salinity (https://www.lockheedmartin.com/en-us/products/oceanographic-instrumentation.html). During the two surveys, a total of 263 CTD stations and 98 XCTD casts were occupied. Note that most of the *Healy's* CTD stations only extended to 800 m off the shelf, which is deep enough to capture the layer of Atlantic-origin water.

2.1.2. Nutrient and oxygen isotope data

A total of 957 nutrient samples from 130 stations were collected from the Niskin bottles during the *Healy* survey (Fig. 2) and analyzed at the Marine and Freshwater Research Institute of Iceland. Typical sampling depths were surface, 25 m, 50 m, and every 100 m below 100 m. The nutrient data include nitrate, nitrite, phosphate, and silicate. Concentrations of nitrate + nitrite, phosphate, and silicate were determined from the samples (preserved with chloroform and stored in the dark at 4 °C) using a Seal Analytical AutoAnalyzer AA3. Estimations for

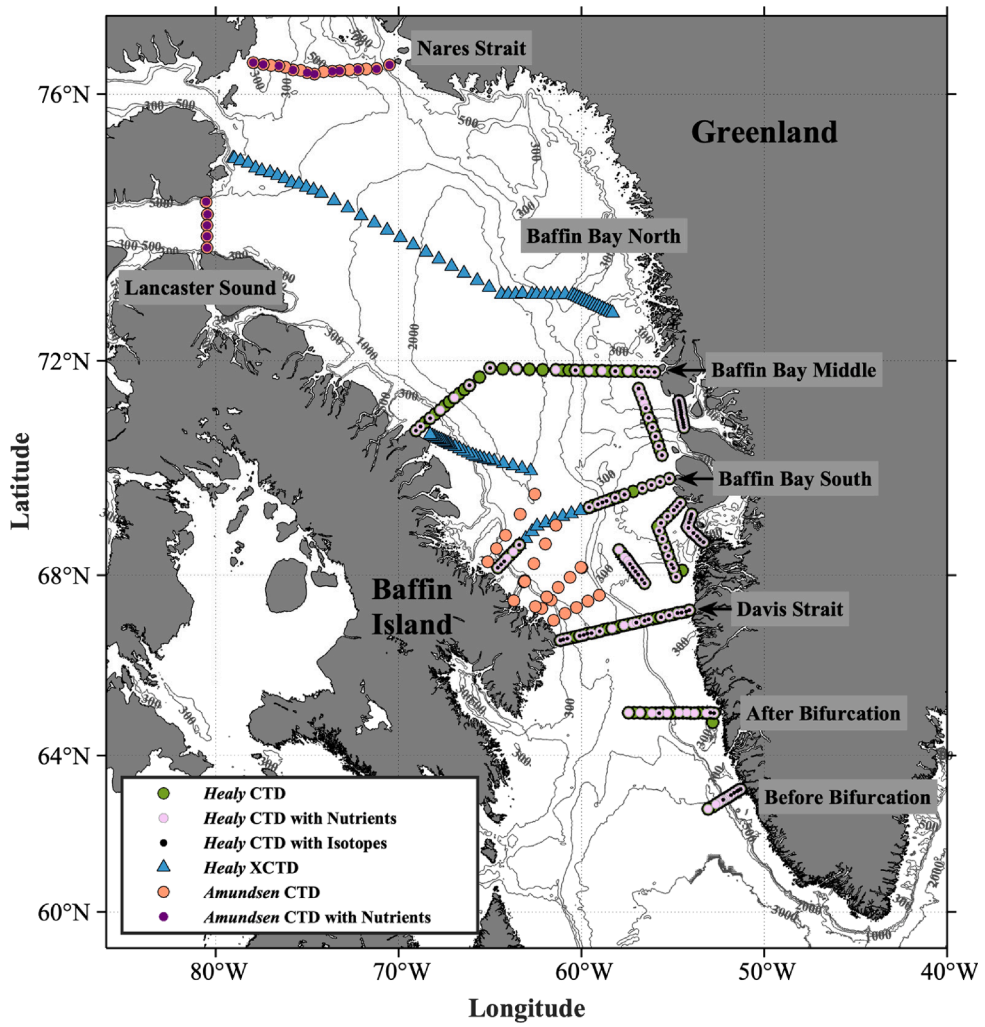

Fig. 2. Hydrographic, nutrient, and isotope stations occupied during the two Baffin Bay surveys in 2021 (*Healy* survey from 17 September to 4 October and *Amundsen* survey from 17 August to 5 September). The names of the sections used in the study are indicated. The bathymetry (gray contours) is from ETOPO1.

uncertainty were calculated according to the OSPAR's Joint Assessment and Monitoring Program Guidelines (Agreement 2011–3, https://www.ospar.org/convention/agreements/page6?q=OSPA) and based on use of certified and internal reference materials, duplicate measurements, and limits of detection (LoD). LoD and uncertainty for these analyses are as follows: nitrate + nitrite, LoD=0.08 μM, uncertainty = ± 2.5 %; phosphate, LoD=0.006 μM, uncertainty = ± 2.5 %; silicate, LoD=0.015 μM, uncertainty = ± 1.8 %. For the *Amundsen* survey, 410 nutrient samples from 25 stations were taken from the Niskin bottles. Working standards were prepared at each station and checked against certified reference material (KANSO CRM) inserted into the sample runs. Concentrations of nitrate + nitrite, nitrite, phosphate, and silicate were determined within a few hours after collection using a Bran and Luebbe AutoAnalyzer III. Analytical detection limits were 0.03 μM for nitrate, 0.02 μM for nitrite, 0.05 μM for phosphate, and 0.1 μM for silicate. The precision of triplicate nutrient measurements under the range of concentrations observed was the same as or better than the detection limit for each nutrient. Hereafter we equate nitrate + nitrite to nitrate for simplification since the concentration of nitrite is generally two orders of magnitude smaller than that of nitrate.

To complement the nutrient sampling, oxygen isotope ($\delta^{18}O$) measurements were done at a spatially representative subset of the stations. A total of 671 samples from 97 stations were collected from the Niskin bottles from all typical sampling depths at a given station, as described above. Water samples for oxygen isotopic measurements were collected in 40 mL HDPE bottles and refrigerated until the end of the cruise and shipped to the University of Oulu for analysis. Samples were analyzed on a Picarro L2130-i analyzer for their $\delta^{18}O$ value, and all isotopic values presented here are computed on the VSMOW-SLAP scale. The analytical uncertainty (1σ) for $\delta^{18}O$ is 0.1 ‰.

2.1.3. Velocity data

Shipboard acoustic Doppler current profiler (SADCP) data were collected during the *Healy* survey using an Ocean Surveyor (OS) 150-kHz unit and 75-kHz unit. The former collected data in 4-m bins and had a depth range of approximately 80 m, while the latter collected data in 8-m bins with a depth range up to 400 m. Pre-cruise ADCP performance was evaluated by personnel at the University of Hawaii during the annual shake-down cruise at the beginning of the season. The raw data were collected and processed using the UHDAS software package (https://currents.soest.hawaii.edu, Firing et al., 2010; 2012). The processing included water track calibrations, which compared ship accelerations as recorded by GPS and ship-relative ADCP measurements (this method reduces loss of pings compared with bottom track calibrations). Accurate ship's heading, essential for high quality SADCP data, was provided by an inertial navigation/GPS assist heading device (POSMV and Seapath). The UHDAS software applies single ping editing during acquisition that has been tuned to address minor acoustic interference from other sonars. Subsequent manual data processing included visual editing of the 5-minute ensemble-averaged profiles to address

occasional outliers. The fully edited datasets from the two ADCPs were combined into a single product to maximize the vertical resolution. In regions of overlap, weight factors that varied linearly from 1 to 0 over the top 100 m favored the OS150 in the shallow portion of the profiles. Finally, the barotropic tidal signal was removed from each velocity profile using the Oregon State University TPXO9-V3 model (https://www.tpxo.net/global/tpxo9-atlas). Additional details of the SADCP data processing can be found in Huang et al. (2021) and Pickart et al. (2023). During the *Amundsen* survey, a WHM300-RDI lowered acoustic Doppler current profiler (LADCP) was installed on the rosette to measure velocity. The data were processed by the *Amundsen* science group (Amundsen Science Data Collection, 2021), and the barotropic tides were subsequently removed using the Oregon State University model.

Laplacian-spline interpolation (Pickart & Smethie, 1998) was used to construct vertical sections of potential temperature and potential density (referenced to the sea surface), practical salinity, nutrients, oxygen isotope, and absolute geostrophic velocity. The absolute geostrophic velocities were calculated by referencing the CTD-derived thermal wind using the SADCP/LADCP data, following the procedure described in Huang et al. (2021). The uncertainty in velocity is estimated to be 2 cm/s (Huang et al., 2021; Huang et al., 2023a; Pickart et al., 2023). The resolution of the vertical sections is 10 m in depth and 5 km in distance.

2.2. Ocean reanalysis velocity data

Velocity data from the reanalysis product ARMORD (Guinehut et al., 2012; Mulet et al., 2012) were used to investigate the variability of the basin-scale circulation in Baffin Bay. This product provides monthly-averaged temperature, salinity, geopotential height, and geostrophic velocity data for the global ocean with 1/4° latitude by 1/4° longitude spatial resolution from 1993 onward. Its hydrographic fields are based on a combination of satellite and in-situ data, and the geostrophic velocity is obtained by referencing the thermal wind shear (computed using the hydrographic fields) to the surface velocity derived from the satellite altimetry. Additional details of this product, including its quality information, can be found at https://data.marine.copernicus.eu/product/MULTIOBS_GLO_PHY_TSUV_3D_MYNRT_015_012.
ARMORD has previously been shown to accurately reproduce the circulation in the subpolar North Atlantic and Nordic Seas (Bashmachnikov et al., 2021; Huang et al., 2023b).

2.3. Reanalysis wind data

The monthly-averaged wind data used in this study (1993–2021) were obtained from the European Centre for Medium–Range Weather Forecasts reanalysis version5 (ERA5), with 1/4° spatial resolution (Hersbach et al., 2020; https://www.ecmwf.int/en/forecasts/datasets/reanalysis-datasets/era5). The ERA5 data have been widely used in studies of the subpolar North Atlantic and have been shown to compare well with meteorological buoy observations in the Nordic Seas (Renfrew et al., 2021).

2.4. Water mass analysis using the potential density-potential spicity framework

The potential density-potential spicity (σ_0-π_0) coordinate system (Huang et al., 2018) was used in the identification of the water masses in Baffin Bay. The potential spicity (π_0) is a thermodynamic variable whose contours are orthogonal to potential density (σ_0) contours in potential temperature-salinity space, hence π_0 contains information regarding temperature and salinity not included in σ_0. Since the equation of state of seawater is nonlinear, there can be small uncertainties in σ_0 and π_0 (e.g., the cabbeling effect of σ_0) when quantifying the mixing of different water masses, which are unimportant in this analysis.

All water parcels collected during the two surveys were classified by comparing their distance to the defined endmember water masses in σ_0-π_0 space. The smaller the distance, the closer the water parcel is to the dominant endmember water mass. This metric has been successfully applied in previous studies to document water masses in the high latitude North Atlantic (Huang et al., 2020; Huang et al., 2023a; Huang et al., 2023b), where the upper layer temperature usually varies with a bigger range than salinity but the density of seawater depends more on salinity. Compared with potential temperature-salinity (θ-S) space, the distance quantification in σ_0-π_0 space is more meaningful due to the fact that σ_0 and π_0 are orthogonal to each other and their gradients are comparable (which is not the case for θ and S).

2.5. Pacific-origin and freshwater composition

The nutrient, oxygen isotope, and salinity data collected during the *Healy* survey were combined to quantify the fractions of Pacific water, meteoric water (MW), and sea-ice melt water (SIM) in Baffin Bay. As the Pacific water traverses the Arctic Ocean, its nitrate is depleted due to biological processes such as microbial denitrification (Jones et al., 1998; Tremblay et al., 2015), which results in lower nitrate concentration relative to those of phosphate. Following previous studies (Jones et al., 2003; Jones et al., 2008; Yamamoto-Kawai et al., 2008; Sutherland et al., 2009; Alkire et al., 2019), the Pacific water fraction was first computed based on the nitrate-phosphate relationship using the nutrient data:

$$f_{PAC} = \frac{PO_4^{obs} - PO_4^{ATL}}{PO_4^{PAC} - PO_4^{ATL}}, \tag{1}$$

where the PO_4^{obs} is the observed phosphate value, and PO_4^{ATL} (PO_4^{PAC}) is the phosphate value the sample would have if it were purely Atlantic (Pacific) water, determined from the observed nitrate value and the nitrate-phosphate relationship of purely Atlantic and Pacific water. The second step is to differentiate the contribution between oceanic water (combination of Atlantic and Pacific waters), meteoric water, and sea-ice melt water, according to the following set of conservation equations based on the salinity and $\delta^{18}O$ data:

$$f_{ATL} + f_{PAC} + f_{MW} + f_{SIM} = 1 \tag{2}$$

$$O^{18}_{ATL} * f_{ATL} + O^{18}_{PAC} * f_{PAC} + O^{18}_{MW} * f_{MW} + O^{18}_{SIM} * f_{SIM} = O^{18}_{obs} \tag{3}$$

$$S_{ATL} * f_{ATL} + S_{PAC} * f_{PAC} + S_{MW} * f_{MW} + S_{SIM} * f_{SIM} = S_{obs}, \tag{4}$$

where O^{18}_{obs} is the observed $\delta^{18}O$ value, S_{obs} is the observed salinity value, f_{ATL}, f_{MW}, f_{SIM} are fraction of Atlantic, meteoric, and sea-ice melt waters, respectively, and O^{18}_{ATL}, O^{18}_{PAC}, O^{18}_{MW}, O^{18}_{SIM} (S_{ATL}, S_{PAC}, S_{MW}, and S_{SIM}) are $\delta^{18}O$ (salinity) values of Atlantic, Pacific, meteoric and sea-ice melt endmembers, respectively. Note that equation (1) does not account for the contribution due to meteoric water and sea-ice meltwater, which means that the Pacific fraction needs to be adjusted accordingly; in particular, it needs to be multiplied by the fraction of oceanic water (Yamamoto-Kawai et al., 2008; Alkire et al., 2018):

$$f^*_{PAC} = f_{PAC} * (1 - f_{MW} - f_{SIM}) \tag{5}$$

where f^*_{PAC} is the final estimate of the Pacific water fraction. Details of the nitrate-phosphate relationship source lines and endmember properties are provided in Section 3.2.2, together with the uncertainties of the estimated water mass fractions.

3. Results

3.1. Water masses and their definitions

We begin by presenting the occurrence of the different water masses

in Baffin Bay in potential temperature-salinity (θ-S) space, using the hydrographic data collected from the two surveys (Fig. 3a). Following previous studies (Curry et al., 2014; Mortensen et al., 2018; Pickart et al., 2023), four main water masses were identified: (1) warm and salty West Greenland Irminger Water (WGIW; i.e., the Atlantic-origin water advected in the WGC); (2) cold and relatively fresh Polar Water (cold PW, which is referred to as Arctic Water in Curry et al. (2014) and Baffin Bay Polar Water in Mortensen et al. (2018)); (3) warm Polar Water (warm PW) which has a similar salinity as cold PW but is characterized by warmer temperatures; and (4) fresh sea-ice meltwater and meteoric water (MWM).[1] In θ-S space, most of the water (more than 80 %) was distributed along the ridge of maximum occurrence frequency between the WGIW and cold PW, indicating the dominant role of these two water masses (as well as the mixing between them). Note that the water in the 600–1000 m depth range in Baffin Bay is relatively homogeneous (standard deviation of temperature < 0.4 °C and salinity < 0.04), hereafter referred to as Baffin Bay Mode Water (BBMW, indicated by the open square in Fig. 3a). This water is located close to the mixing line between the WGIW and cold PW. While the occurrence of warm PW and MWM is much lower, there are visible ridges of maximum occurrence between them and the cold PW, as well as between the two of them. By selecting the endpoints along the maximum occurrence ridges, we determined the θ-S properties of four endmember water masses (the red stars in Fig. 3a and Table 1).

There are notable differences in the nutrient concentrations and their ratios for the four endmember water masses (Table 2). The mean concentration was obtained by averaging the nutrient values of the water masses whose temperature and salinity are similar to the endmember (temperature difference < 0.2 °C and salinity difference < 0.2). Consistent with previous studies (Jones et al., 2003; Sutherland et al., 2009), the WGIW endmember is distinguished by low concentrations of phosphate and silicate relative to high concentrations of nitrate (the mean concentration of nitrate is 14.96 ± 0.29 *umol*/kg; N:Si:P=14.6:7.4:1). By contrast, higher concentrations of phosphate and silicate relative to lower concentrations of nitrate occurred for the cold PW endmember (the mean concentration of nitrate is 9.86 ± 0.35 *umol*/kg; N:Si:P=9.5:11.8:1), which is similar for the Pacific source water flowing through Bering Strait into the Arctic Ocean (Jones et al., 1998). Such depleted nitrate concentrations also exist for the Warm PW and MWM endmembers (the mean concentration of nitrate for the latter is 0.18 ± 0.13 *umol*/kg, which is even lower than that of phosphate for this endmember).

Next, we investigated the distribution of water masses in potential density-potential spicity (σ_0-π_0) space (Fig. 3b, where the endmembers obtained from θ-S space were projected and indicated by the black stars in σ_0-π_0 space). Here we focus on the upper 600 m where the four water masses are mainly located. As described in Section 2.4, the advantage of working in σ_0-π_0 space is that we can more meaningfully determine how similar two water parcels are. By computing the σ_0-π_0 distances of a given water parcel to the four endmembers, the closest endmember can be quantified, and the dominant role of this endmember documented. Following this approach, the WGIW, warm PW, cold PW, and MWM dominant water masses are indicated by red, blue, purple, and green colors in Fig. 3b. The darker the color, the smaller the σ_0-π_0 distance to the dominant endmember and hence the more similar the water is to the endmember. Water parcels whose distances to two or three endmembers are comparable and large (σ_0-π_0 distances > 0.6 kg/m^3), are considered as transition water (indicated by grey color in Fig. 3b). Two types of transition water are identified: TrW1 is a mixture between WGIW, cold PW, and warm PW; and TrW2 is a mixture between warm PW, cold PW, and MWM. Compared with the water masses defined by the temperature and salinity boundaries, the σ_0-π_0 approach is more accurate for identifying the transition water. Note that the BBMW has similar properties to the densest portion of TrW1.

[1] As explained in Section 2.5 we can use the tracer data to distinguish these two sources of freshwater. However, the spatial resolution of the tracer measurements is much coarser than the CTD data, and here we are using the CTD data to map out detailed water mass distributions; hence, the two freshwater sources are combined for this purpose. Also, we note that the MWM here represents seawater that is significantly influenced by the freshwater sources, not the pure freshwater.

3.2. Water mass distributions

In this study, different approaches were applied to document the water mass distributions. We firstly used the high-resolution CTD data in the σ_0-π_0 framework (Section 3.2.1) which was effective for distinguishing the four main water masses in Baffin Bay. We then used the lower resolution chemical data to further investigate the sources of PW as well as freshwater composition (Section 3.2.2), which can't be done with the CTD data.

3.2.1. The potential density-potential spicity framework

The water property identification approach in σ_0-π_0 space was applied to document the geographical distribution of the four dominant water masses. Fig. 3c provides an example of how this approach works to distinguish the water masses across Davis Strait. Comparing the vertical sections of temperature, salinity, and σ_0-π_0 distance, one can clearly see the thin, fresh MWM layer at the surface, the dominance of the cold PW layer in the upper 300 m of the water column, the warm PW layer residing above the west Greenland shelf, and the warm and salty WGIW centered at 300–600 m depth on the west Greenland slope. The two transition waters are located between the boundary of the corresponding water masses. We note that the distribution of dominant water masses is not sensitive to different choices of thresholds for the σ_0-π_0 distances: the smaller the threshold, the more distinguished the four water masses are (with more transition waters located between the dominant water masses).

The same approach in σ_0-π_0 space can be used to construct a geographical map of the thickness of the four dominant water masses (Fig. 4, applied to the 0–600 m depth range). A thin and fresh surface layer of MWM occupies the upper 30 m over much of the bay (Fig. 4a), except for some areas of the west Greenland shelf where warm PW was more dominant. Interestingly, the largest presence of MWM is found along the coast of Baffin Island (hotspots of thickness > 40 m), rather than along the Greenland coast where large glaciers reside. One possible explanation for this is that the freshwater emanating from the glaciers is diluted by the salty Atlantic-origin water flowing along the west Greenland shelf and slope.

The presence of cold PW water dominated the other three water masses in the upper 600 m over the central and western portions of the bay (note that different color scales were used for the top and bottom panels in Fig. 4). By contrast, WGIW was the main water mass found along the continental slope of the northern Labrador Sea, although its thickness decreased drastically north of Davis Strait (Fig. 4d). This implies that, during the time period of observation, only a small amount of WGIW was being transported with the WGC into Baffin Bay, and/or it was diluted quickly due to mixing with the cold PW. Notably, warm and salty WGIW was found in the deep troughs connected to the two west Greenland glacier fjords that were sampled (near 68°N and 72°N), which can play an important role in regulating the melting of glaciers in this region (Carroll et al., 2018).

In addition to the layer thickness, we computed the layer mean temperature and salinity for the cold PW and WGIW dominant water masses (Fig. 5). The coldest and freshest cold PW (temperature < -1 °C and salinity < 33) was found along the western shelf and slope of Baffin Bay, while there was a less pronounced signature of this water mass (–1 to –0.5 °C) near the eastern slope of the bay. This is likely due to recirculation of cold PW in Baffin Bay, which is investigated in Section 3.4. Consistent with its layer thickness distribution, the temperature and

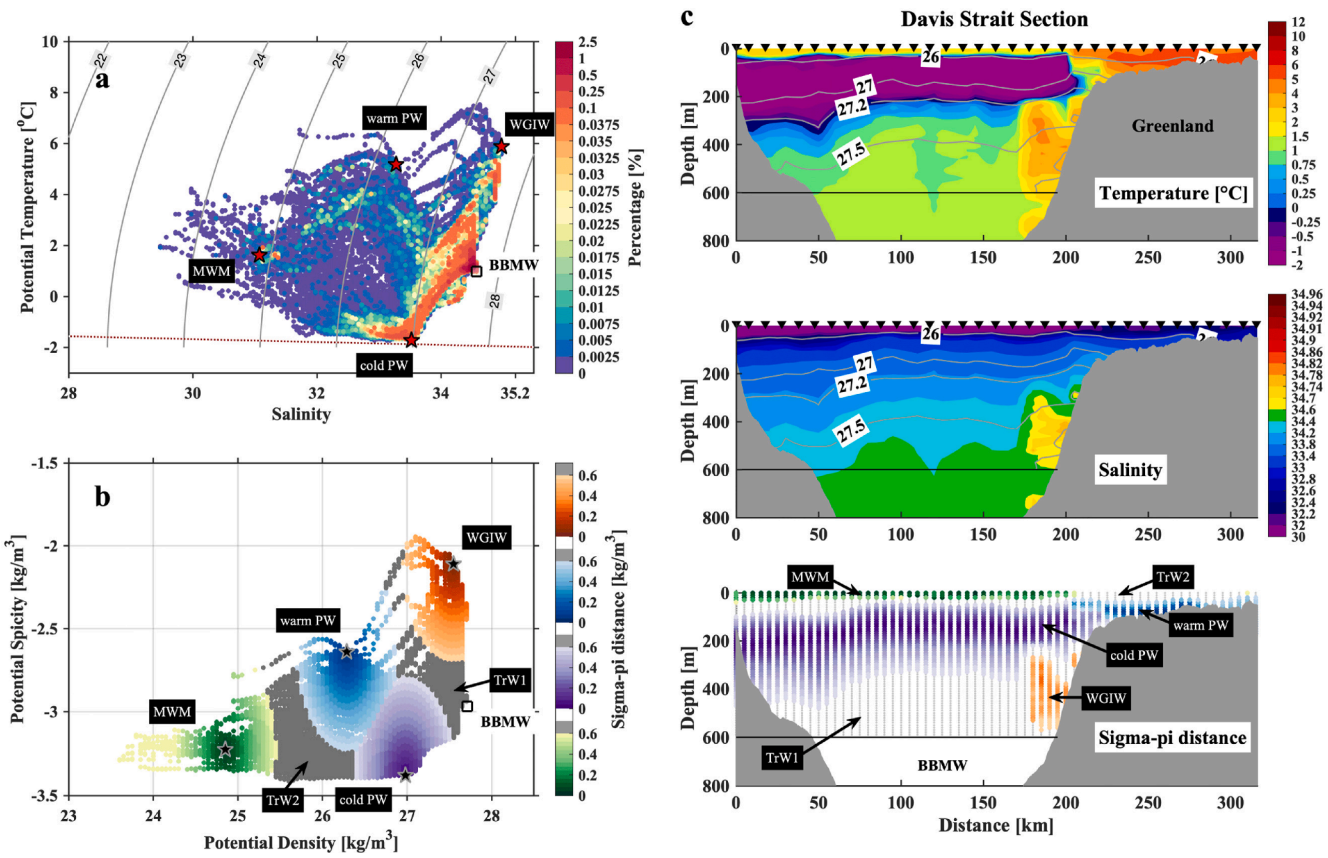

Fig. 3. (a) Potential temperature-practical salinity diagram for the upper 800 m of all the stations occupied during the *Healy* and *Amundsen* surveys in 2021. The color indicates the percentage of data within bins of 0.05 °C in temperature by 0.05 in salinity. The gray contours are potential density (kg/m^3). The four chosen endmembers are indicated by the red stars: warm Polar Water (warm PW), cold Polar Water (cold PW), West Greenland Irminger Water (WGIW), and Sea-ice Meltwater and Meteoric Water (MWM). The Baffin Bay Mode Water (BBMW), which represents the relatively homogeneous water in the 600–1000 m depth range in Baffin Bay (standard deviation of temperature < 0.4 °C and salinity < 0.04) is indicated by the open square. The freezing line is denoted by the red dashed line. (b) potential density-potential spicity (σ_0-π_0) diagram with the four chosen endmembers indicated by black stars (upper 600 m of water column). The WGIW, warm PW, cold PW, and MWM dominant water are distinguished by orange, blue, purple, and green colors, respectively. The two transition waters are shown in gray (see text). (c) Vertical sections of potential temperature (top), practical salinity (middle), and σ_0-π_0 distance to the dominant water masses (bottom) for the Davis Strait section. The gray contours are potential density (kg/m^3). The bottom depth is from *Healy's* echosounder. The horizontal black line indicates the 600 m depth.

Table 1
Water mass and endmember definitions used in calculating the potential density-potential spicity (σ_0-π_0) distance.

Water mass	Abbreviation	Potential temperature of endmember (θ, °C)	Practical salinity of endmember (S)
West Greenland Irminger Water	WGIW	5.9	34.98
Cold Polar Water	Cold PW	−1.7	33.5
Warm Polar Water	Warm PW	5.2	33.3
Sea-ice Meltwater and Meteoric Water	MWM	1.6	31.1
Transition Water type 1	TrW1		
Transition Water type 2	TrW2		
Baffin Bay Mode Water	BBMW		

salinity of the WGIW along the west Greenland slope is strongly moderated progressing to the north as the water becomes colder and fresher. This is seen as well in the vertical sections of hydrographic properties and absolute geostrophic velocity for each of the *Healy* transects (Fig. 6). Furthermore, there are striking changes in the hydrographic and velocity structure from the Before Bifurcation section to the Davis Strait section. A more detailed description of the vertical sections is presented below in Sections 3.3 and 3.4.

Table 2
Mean nutrient concentrations (*umol*/kg) of four endmember water masses. The mean concentration was obtained by averaging the nutrient values of water masses whose temperature and salinity are similar to the endmember (temperature difference < 0.2 °C and salinity difference < 0.2). The error indicates the standard deviation.

Water mass	Nitrate (N)	Silicate (Si)	Phosphate (P)	N:Si:P ratio
WGIW	14.96 ± 0.29	7.57 ± 0.45	1.03 ± 0.01	14.6:7.4:1
Cold PW	9.86 ± 0.35	12.2 ± 1.27	1.04 ± 0.05	9.5:11.8:1
Warm PW	1.94 ± 0.33	3.54 ± 0.87	0.51 ± 0.05	3.8:7.0:1
MWM	0.18 ± 0.13	2.56 ± 0.55	0.60 ± 0.02	0.3:4.3:1

3.2.2. *Nutrient and oxygen isotope derived water mass composition*

The nutrient and oxygen isotope data collected during the two surveys provide the opportunity to delve further into the details of the water mass composition in Baffin Bay. We present the vertical sections of nitrate, phosphate, and silicate (Fig. 7) for four of the *Healy* transects. Not surprisingly, the surface waters of Baffin Bay, comprised mostly of

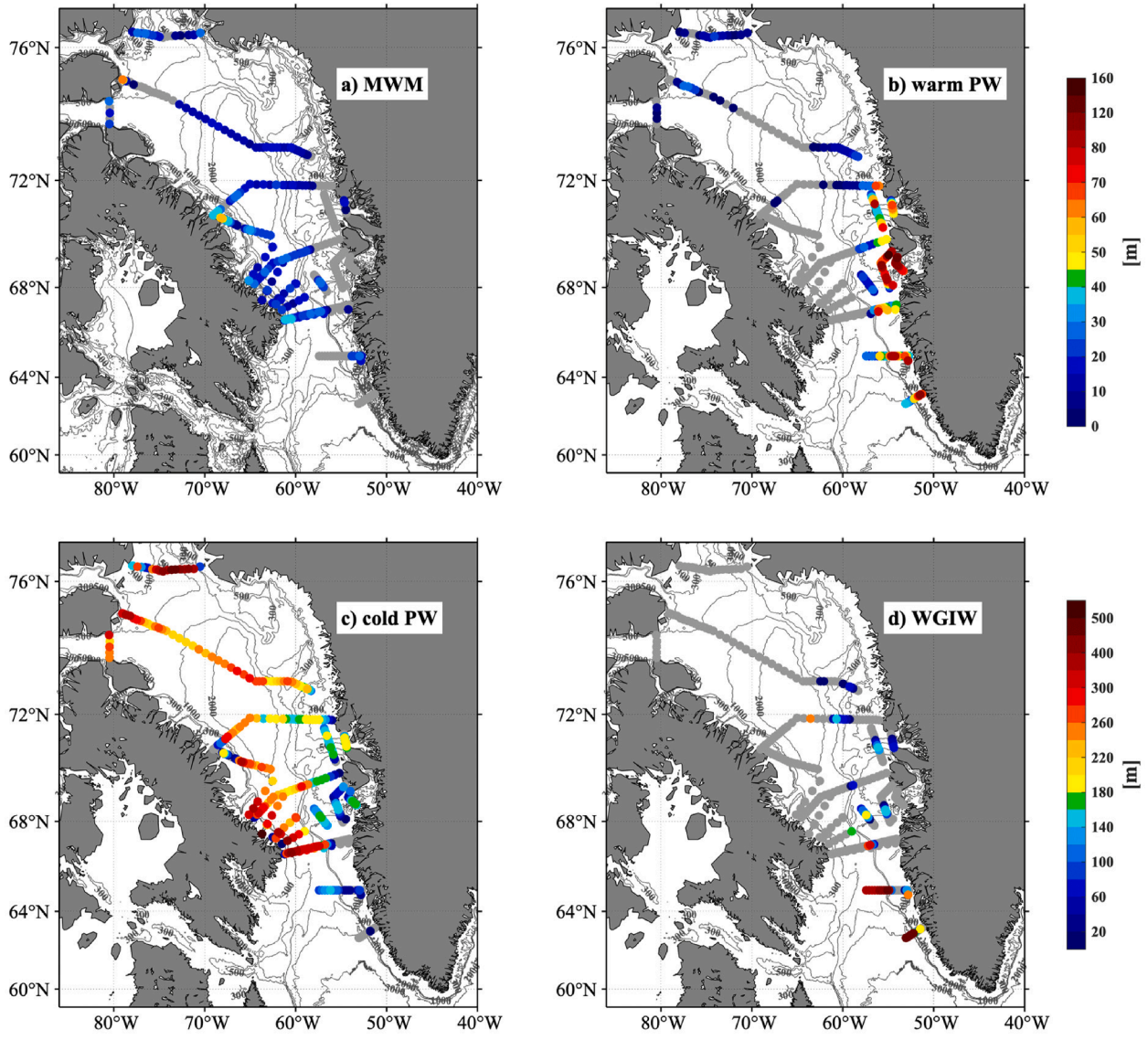

Fig. 4. Thickness of (a) MWM, (b) warm PW, (c) cold PW, and (d) WGIW dominant water in the upper 600 m of the water column. Stations where the dominant water is not found are shown by gray circles. Note that different color scales are used for the MWM and warm PW (0–160 m), and for the cold PW and WGIW (0–600 m). The bathymetry (gray contours) is from ETOPO1.

MWM and warm PW, were characterized by low concentrations of nutrients. In general, the concentrations of all the nutrients increase with depth; however, low concentrations of phosphate and silicate were found near 400 m on the west Greenland slope for the Davis Strait section, where the WGIW enters Baffin Bay. In addition, higher concentrations of phosphate and silicate were found on the eastern side of the Davis Strait section, from approximately 160–180 km, indicating again the recirculation of cold PW in the southern bay. Overall, the nutrient signals agree well with the hydrographic characterizations of the dominant water masses in Baffin Bay.

Previous studies have demonstrated that high-latitude meteoric water typically has a very low $\delta^{18}O$ value (near −21 ‰), while sea-ice meltwater has a relatively high value (roughly 1 ‰) (Ekwurzel et al., 2001; Sutherland et al., 2009). These differences allow further separation of the composition of the different water masses measured during our surveys. As discussed in Section 2.5, endmembers of phosphate, $\delta^{18}O$, and salinity are required for this quantification, which are provided as follows. The endmembers of phosphate corresponding to a given observed nitrate value were obtained by using the purely Atlantic and Pacific water source lines from Jones et al. (2003) (Fig. 8a). The endmembers of $\delta^{18}O$ and salinity for meteoric water and sea-ice meltwater, respectively, are from Sutherland et al. (2009) (Table 3). The salinity of the Atlantic water endmember was taken to be the maximum salinity measured during the *Healy* survey (34.98), and that for the Pacific water was taken to be 32.6 based on climatological hydrographic data from Bering Strait (Pickart et al., 2023). The endmembers of $\delta^{18}O$ for Atlantic and Pacific waters were determined by the regression relationship of $\delta^{18}O$ and salinity from the 2021 *Healy* survey (Fig. 8b and Table 3).

The resulting fractions of Pacific water (f_{PAC}), meteoric water (f_{MW}), and sea-ice meltwater (f_{SIM}) for the sections occupied during the *Healy* survey are shown in Figs. 8 and 9. The AW fraction is not shown to avoid confusion with the subtropical-origin WGIW in the σ_0-π_0 framework (the AW source line from Jones et al. 2003 was obtain by using data from the high Arctic Ocean, where the AW has much colder temperature compared with the subtropical-origin WGIW). Here we focus on the upper 500 m of water column to avoid the impact of local remineralization and denitrification on the estimation of f_{PAC} in deep waters (Tremblay et al., 2015). The uncertainties of f_{PAC}, f_{SIM}, and f_{MW} are 0.1, 0.03, and 0.03, respectively (Jones et al., 2003; Yamamoto-Kawai et al.,

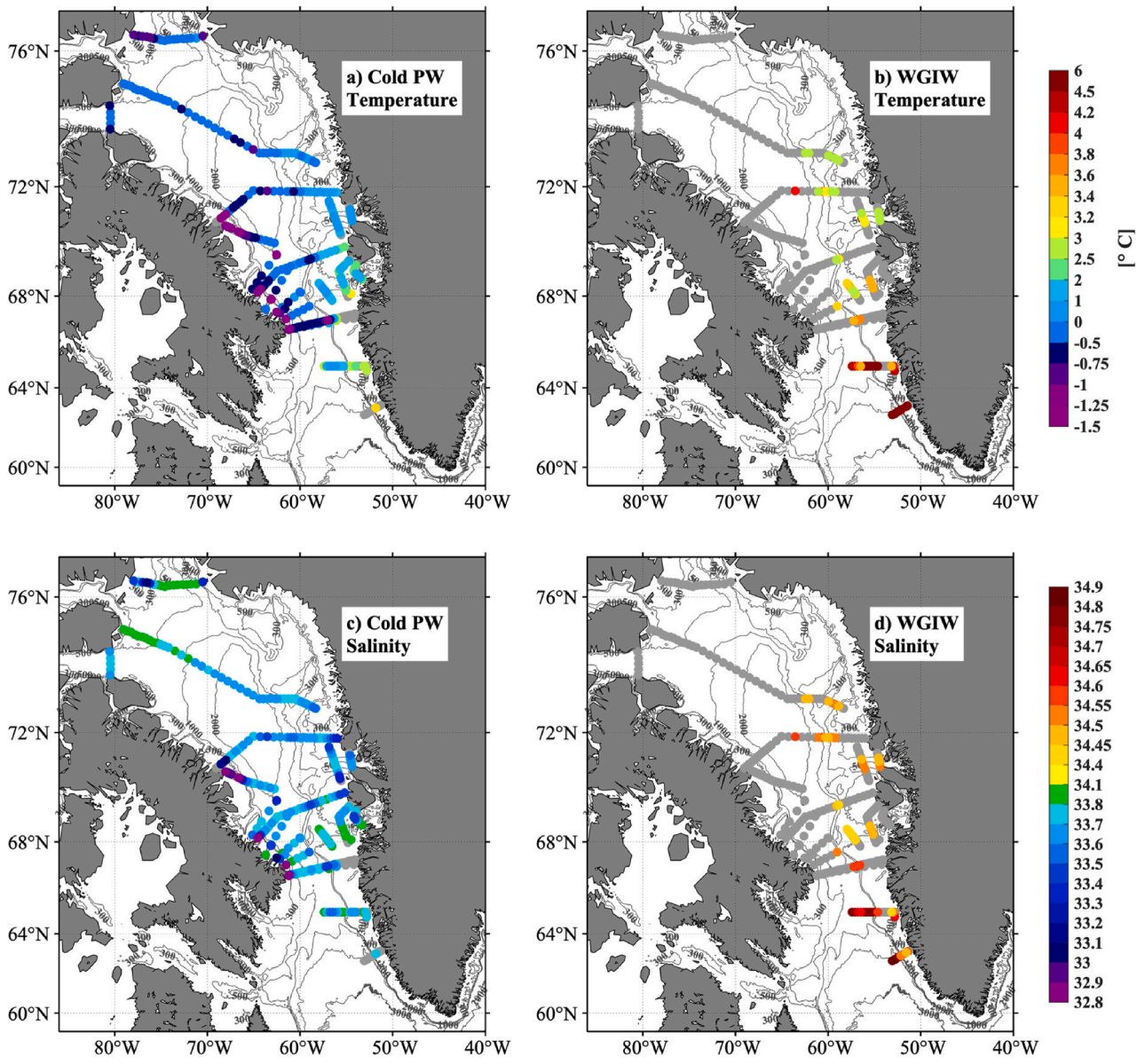

Fig. 5. Mean potential temperature (top) and salinity (bottom) for the cold PW (left) and WGIW (right) dominant water at each station (upper 600 m of the water column). Stations where the cold PW or WGIW dominant water is not found are shown by gray circles. The bathymetry (gray contours) is from ETOPO1.

2008). The former is mainly associated with the uncertainties of purely Atlantic and Pacific source lines, while the latter two are due to uncertainties in the range of end-member values (see Table 3). Our results reveal that the Pacific water fraction is high (>0.5) from the surface to 200 m, with the highest percentage on the western sides of the sections (Fig. 8c). These values are larger than those calculated along the East Greenland Current from Denmark Strait to Cape Farewell (Sutherland et al., 2009; Dodd et al., 2012), which is not surprising since the pathways of Pacific water through Canadian Arctic Archipelago into Baffin Bay are shorter and more direct. By contrast, the fractions of meteoric water and sea-ice meltwater are much lower (<0.1) throughout Baffin Bay (Fig. 9). This is consistent with the freshwater fractions obtained using tracer measurements in September-October of 2004 in Davis Strait (fraction of meteoric water ranges from 0 to 0.1 and fraction of sea-ice meltwater < 0.02, Azetsu-Scott et al., 2012). Such a low fraction of sea-ice meltwater is not surprising since the data were collected late during the melting season. However, in contrast with Azetsu-Scott et al. (2012), where the fraction of meteoric water is highest on the Greenland shelf, our results show relatively high fractions of surface meteoric water on both sides of the bay.

3.3. *Velocity structure and evolution of water masses along the boundary current*

ADCP velocity data were collected on all of the sections during the *Healy* survey and for the two northern sections during the *Amundsen* survey, allowing us to compute absolute geostrophic velocities (see Section 2.1.3). Fig. 6 (right panels) shows the vertical sections of absolute geostrophic velocity from the *Healy* survey, including the four long sections extending across the entire bay (Davis Strait, Baffin Bay south, Baffin Bay Middle, and Baffin Bay North) and the two short sections across the southwest Greenland shelf and slope (Before Bifurcation and After Bifurcation; see Fig. 2 for the locations of the sections). At the southern-most section (Before Bifurcation), a strong, surface-intensified WGC is present seaward of the shelfbreak (maximum velocity > 50 cm/s). Farther shoreward on the shelf, the northward flowing WGCC is comprised of two weaker cores. The magnitude and location of the WGC and WGCC are consistent with those observed farther south at the

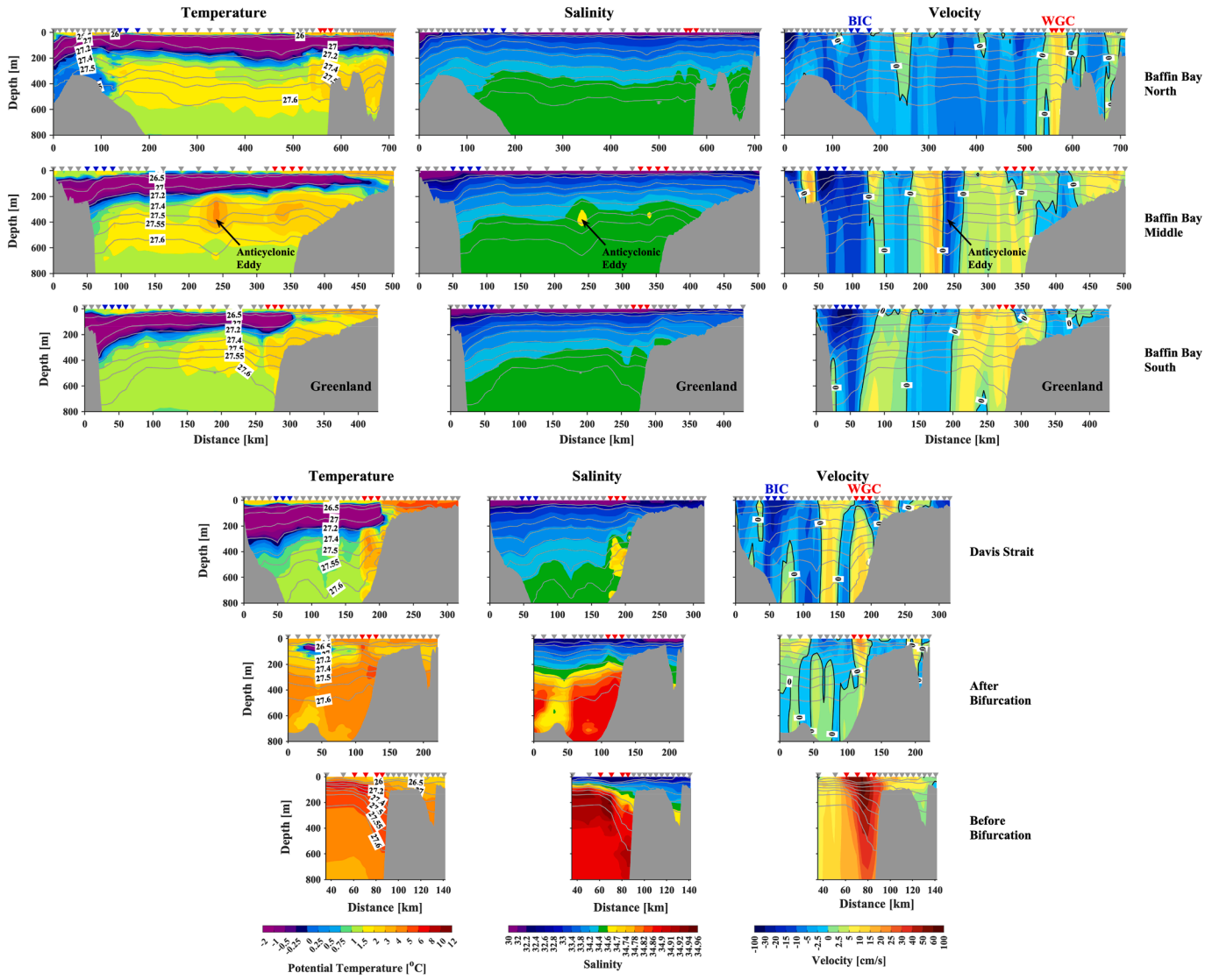

Fig. 6. Vertical sections of potential temperature (left), practical salinity (middle), and absolute geostrophic velocity (right) for six of the *Healy* transects, progressing south to north (bottom to top). See Fig. 2 for the locations of the sections. The stations are indicated by the inverted triangles; those in the WGC and BIC are indicated by the red and blue inverted triangles, respectively (see the text). The gray contours are potential density (kg/m^3), and the black contour is zero velocity. Positive velocities are northward. Note that the color scales are not linear.

Overturning in the Subpolar North Atlantic Program (OSNAP) West mooring line (Pacini et al., 2020; Foukal & Pickart, 2023; see Fig. 1 for the location of the line). At the next section north (After Bifurcation), the WGC is pronouncedly weaker, implying that most of the current was diverted westward across the northern end of the Labrador Sea as part of the bifurcation. As such, only a limited amount of the warm and salty WGIW continued northward towards Baffin Bay. By contrast, the WGCC remained comparable in strength between the two locations.

At Davis Strait the WGC underwent yet another change, transitioning from surface-intensified to bottom-intensified – this bottom intensification remained on all of the eastern boundary sections to the north. The change in vertical structure, likely due to the spread of PW from northern and western Baffin Bay, was concomitant with the subduction of the WGIW underneath the cold PW at Davis Strait (see the temperature section at Davis Strait). In the velocity sections of Fig. 6 we have indicated the stations corresponding to the WGC by red inverted triangles (locations where the northward velocity and subsurface temperature are maximum). Overall, the WGC weakens as it progresses northward in Baffin Bay. The evolution and fate of the WGCC is less clear in our sections. This is in part due to the uncertainty in defining this current. At some of the sections there are two WGCC cores (Before Bifurcation, Davis Strait, Baffin Bay South), while at others there is only one core (After Bifurcation, Baffin Bay Middle, Baffin Bay North). Such variability and lateral meandering of the WGCC is commonly observed farther south at the OSNAP West mooring line (Foukal & Pickart, 2023).

On the western side of Baffin Bay, we have indicated the stations in Fig. 6 corresponding to the BIC by blue inverted triangles (locations of maximum southward velocity associated with strongly sloped isopycnals). This surface-intensified current carries a large amount of cold PW southward, some of it crossing Davis Strait into the Labrador Sea and subpolar North Atlantic. Interestingly, there is evidence of a Baffin Island Coastal Current at some of the sections (which is not addressed further in this study). Overall, the circulation during late-summer to early-fall of 2021 in Baffin Bay was cyclonic, consisting of a bottom-intensified northward-directed current along the eastern continental slope, and a southward-directed, surface-intensified current along the western continental slope. There is also evidence of recirculation from the western side of the basin to the eastern side, which is addressed in Section 3.4. Further discussion about the representativeness of the velocity field measured on our two surveys is provided in Section 3.5.

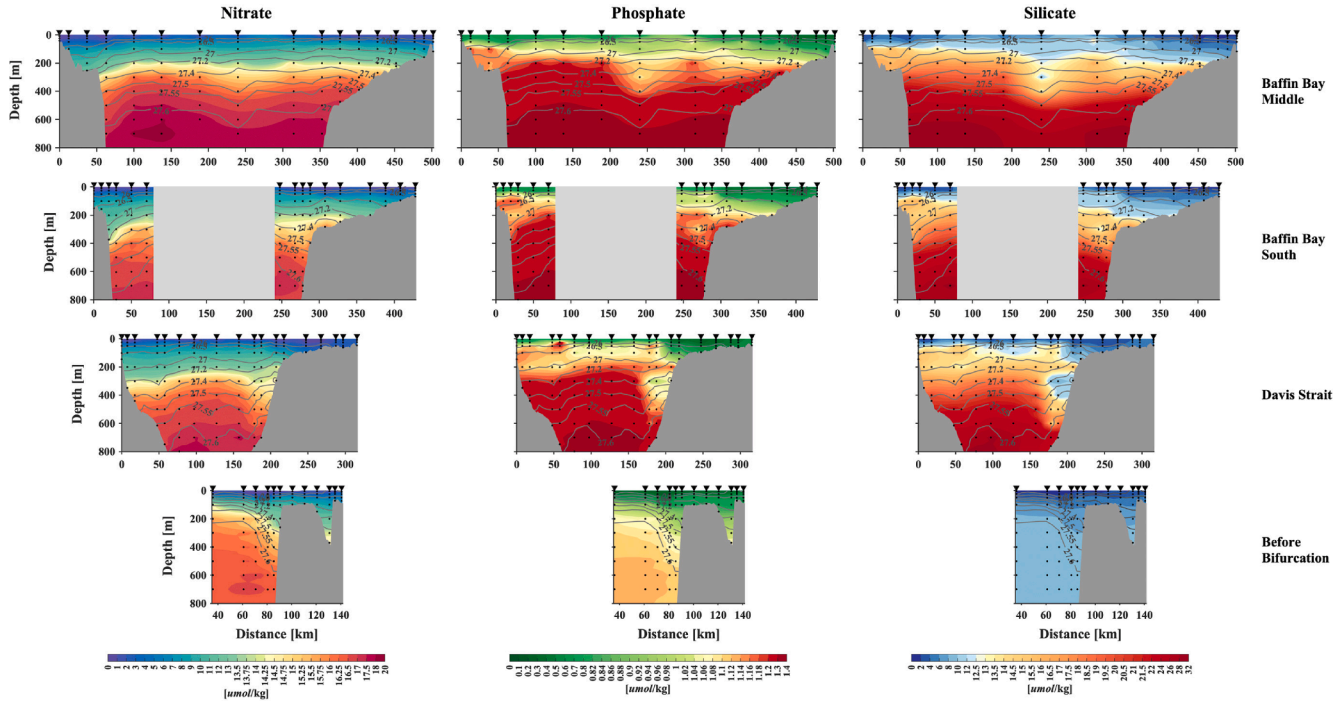

Fig. 7. Vertical sections of nitrate (left), phosphate (middle), and silicate (right) for Baffin Bay Middle, Baffin Bay South, Davis Strait and Before Bifurcation sections (from top to bottom). The sample locations and depths are indicated by the inverted triangles and circles, respectively. The data gap in the interior of Baffin Bay South section is masked in gray. The gray contours are potential density (kg/m^3). Note that the Baffin Bay North section consisted of XCTDs, hence no water sampling.

To document the evolution of the water being advected in the rim current of Baffin Bay, we used the stations within the velocity core (indicated by the red and blue inverted triangles in Fig. 6) to compute a single averaged profile of temperature and salinity at each location. These mean hydrographic profiles are shown in θ-S space in Fig. 10, where the colors change counter-clockwise around the bay from red at the southeastern-most section (Before Bifurcation) to blue at the western side of the Davis Strait section. Along the eastern boundary, significant cooling and freshening occurs as the water progresses from Before Bifurcation to Davis Strait. Farther north in eastern Baffin Bay, the south-to-north water mass transformation was less pronounced and the core of the WGIW (indicated by the subsurface temperature maximum) became gradually colder and less saline following the 27.5 kg/m^3 isopycnal. Such along-isopycnal transformation of the subsurface Atlantic-origin water is similar to that which occurs during the warm months of the year upstream in the East Greenland Current (Håvik et al., 2017). By comparison, the observed change in water mass properties along the western boundary current of Baffin Bay was much smaller, especially from Baffin Bay Middle to Davis Strait where the θ/S properties of the subsurface warm water remained nearly constant. This is consistent with Tang et al. (2004), who demonstrated weak variability of the water masses in southwestern Baffin Bay.

Previous studies have documented the important role of current instabilities and eddy formation in the evolution of water masses along boundary current systems in the high latitude North Atlantic. Both observational and modeling work have demonstrated that the large anticyclonic eddies known as Irminger Rings, spawned from the WGC in the region north of Cape Desolation and south of Davis Strait, transport freshwater in the surface layer and AW at depth toward the interior of the Labrador Sea (Katsman et al., 2004; Bracco et al., 2008; Lilly et al., 2003; de Jong et al., 2014). Smaller boundary current eddies are also believed to be formed along the entire eastern boundary of the Labrador Sea (Katsman et al., 2004; Pacini & Pickart, 2022). However, the occurrence of baroclinic instability and eddy formation farther north in eastern Baffin Bay remains unclear (keeping in mind that the boundary current becomes more weakly baroclinic there compared with southwest Greenland). During the 2021 *Healy* survey, the Baffin Bay Middle section sampled a large anticyclonic eddy in the center of the bay (Fig. 6). This eddy has a subsurface velocity maximum, and its radius (approximately 25 km) is close to the size of Irminger Rings (Gelderloos et al., 2011). While the eddy clearly originated from the eastern boundary current due to its warm and salty core (also corresponding to low concentrations of phosphate and silicate), it is unlikely that it was an Irminger Ring spawned near Cape Desolation, in which case it would have had to cross the bifurcated branch of the WGC in the northern Labrador Sea. Instead, the eddy was likely formed locally in Baffin Bay. At this point it is unknown how common such eddy formation might be; future work is required to quantify the role of this process on the northward evolution of the boundary current in Baffin Bay and the distribution of heat and freshwater in the interior of the bay.

3.4. Volume transport and recirculation

To address the basin-scale circulation in Baffin Bay, for each absolute geostrophic velocity section we calculated the volume transport in the upper 800 m of water column (Fig. 11). While mass is not completely balanced throughout the domain, which is not surprising due to the time it took to complete the two surveys, the transport data nonetheless offer valuable insights regarding the general circulation in the bay. The vectors in Fig. 11 show the magnitude of the transport (in Sv) per 5-km segment, with the northward (westward for the Lancaster Sound section) and southward transports indicated by red and gray colors, respectively (note the different scale for the Before Bifurcation and Lancaster Sound sections).

The cyclonic basin-scale circulation is evident in the transport map: northward flow along the Greenland slope and southward flow along the Baffin Island slope (sometimes there are multiple velocity cores, e.g., at the Davis Strait section). The small transport across the Nares Strait section implies that most of the northward flow on the eastern side of the bay recirculates to the western side; this is likely related to the anomalous cyclonic circulation during the time period of our observation (see Section 3.5). Our results also imply that this recirculated flow

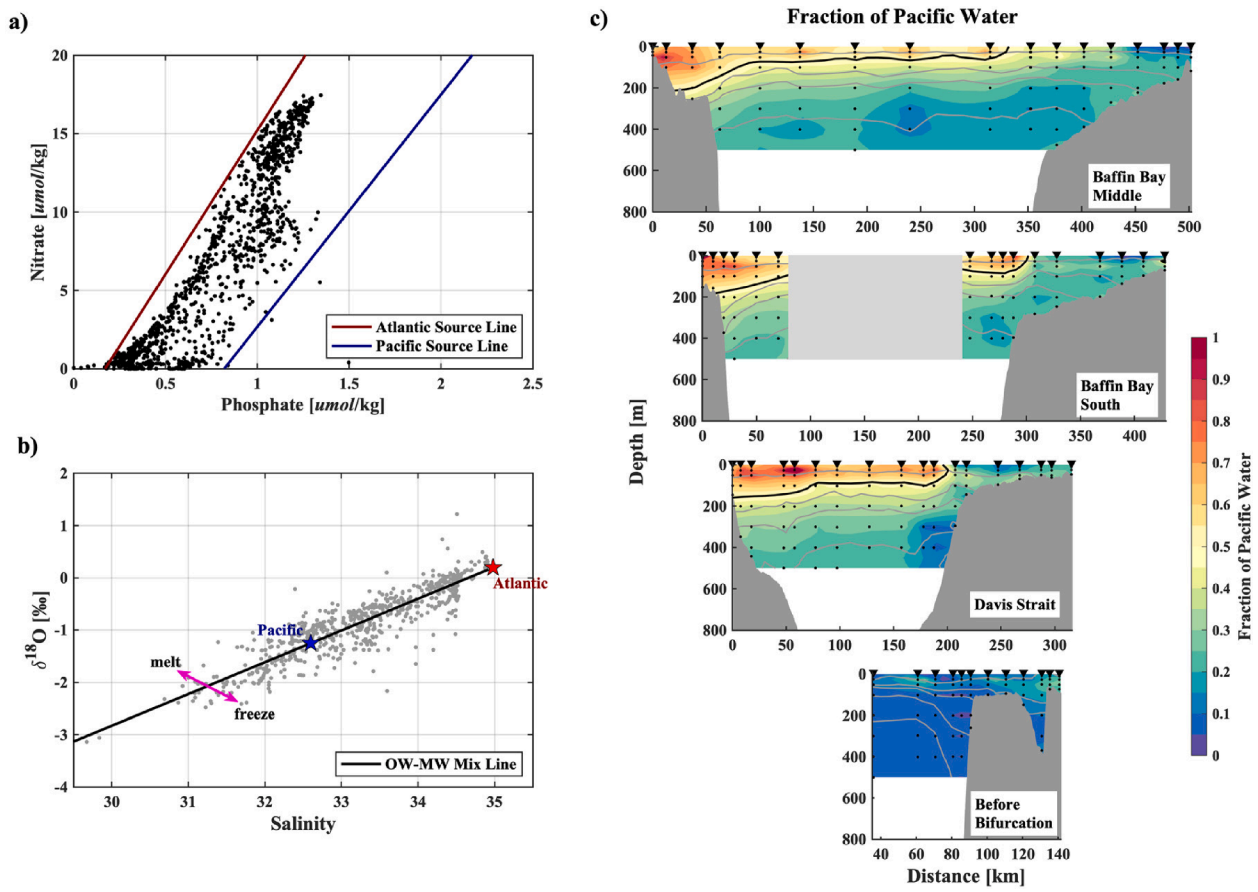

Fig. 8. (a) Phosphate versus nitrate for data collected during the two Baffin Bay surveys (see Section 2.5). The Atlantic and Pacific source lines are from Jones et al. (2003). (b) Salinity versus $\delta^{18}O$ for data collected during the Healy survey. A mixing line between oceanic water (OW) and meteoric water (MW) is obtained by a linear fit ($R^2 = 0.82$, $P<0.05$ for student *t*-test). OW includes Atlantic water (AW) and Pacific water (PW), whose end members are indicated by the stars (see Section 2.5). The arrows indicate the influence of sea ice melt/formation processes. (c) Vertical sections of Pacific water fraction from the Healy survey. The value of 0.5 is indicated by the thick black contour. The data gap in the interior of Baffin Bay South section is masked in gray. Note that the Baffin Bay North section consisted of XCTDs, hence no water sampling.

Table 3
Endmember definitions (and their uncertainties) used in calculating the Pacific water and freshwater composition.

	Atlantic Water	Pacific Water	Meteoric Water	Sea-ice Meltwater
Salinity	34.98	32.6	0	4 (±1)
$\delta^{18}O$ (‰)	0.19 (±0.1)	−1.25 (±0.1)	−21 (±2)	1 (±0.5)

subsequently enters northern Lancaster Sound, while it is the outflow from southern Lancaster Sound that feeds the BIC, consistent with the model results in Wang et al. (2012). We note that our Lancaster Sound section captured an anomalous scenario. Typically, there is a net outflow from the sound into Baffin Bay (Peterson et al., 2012), whereas we measured a small net inflow into the sound. Furthermore, there was a warm subsurface core of AW for both the inflow and outflow of Lancaster Sound, whereas no such core existed for the flow feeding the sound on the northern end of the Baffin Bay North section. The warm core associated with the outflow from Lancaster Sound implies a fairly quick recirculation within the sound. Further support that such warm outflow is not the norm is seen in Fig. 5a indicating that the BIC advects predominantly cold PW in the upper 600 m.

Integrating the transport across the three middle-to-southern Baffin Bay sections occupied during the *Healy* survey (BBM, BBS, and DS) and taking the mean gives −2.3 ± 0.9 Sv, where negative corresponds to southward flow and the error indicates the uncertainty in the transport. This value compares reasonably well to that obtained by Curry et al. (2014) using data from the multi-year mooring array deployed at Davis Strait, −1.6 ± 0.5 Sv (again keeping in mind that our results are quasi-synoptic). Regarding the two northern strait sections occupied during the *Amundsen* survey, there was a net transport of 1.1 ± 0.3 into the bay across Nares Strait and a net transport of −0.2 ± 0.3 Sv out of the bay into Lancaster Sound. The former agrees with the multi-year mooring result (0.9 ± 0.1 Sv) from Münchow (2016), while, as noted above, the latter is at odds with previous observations indicating a net inflow from Lancaster Sound (0.46 ± 0.09 Sv; Peterson et al., 2012).

For each of the four sections that cross the entire bay, a division point (the deepest bottom depth or the turning point of a dogleg section, see the green dots in Fig. 11) was used to separate the transport in the western and eastern portions. These transports, as well as those for the remaining sections across the eastern or western bay, are documented in Fig. 12a. Notably, excluding the BB section (where most of the northward transport is presumably diverted to the west as a result of the well documented bifurcation), there was a south-to-north trend of increasing transport on both sides of the bay. This suggests that some of the southward flow along the western side of the bay recirculates back to the north along the eastern side of the bay. This is consistent with the presence of the double velocity cores between the latitudes of sections DS and BBM, implying that the outer core is associated with recirculated flow (Figs. 6 and 11). While there is not an exact mass balance, these complimentary aspects are compelling.

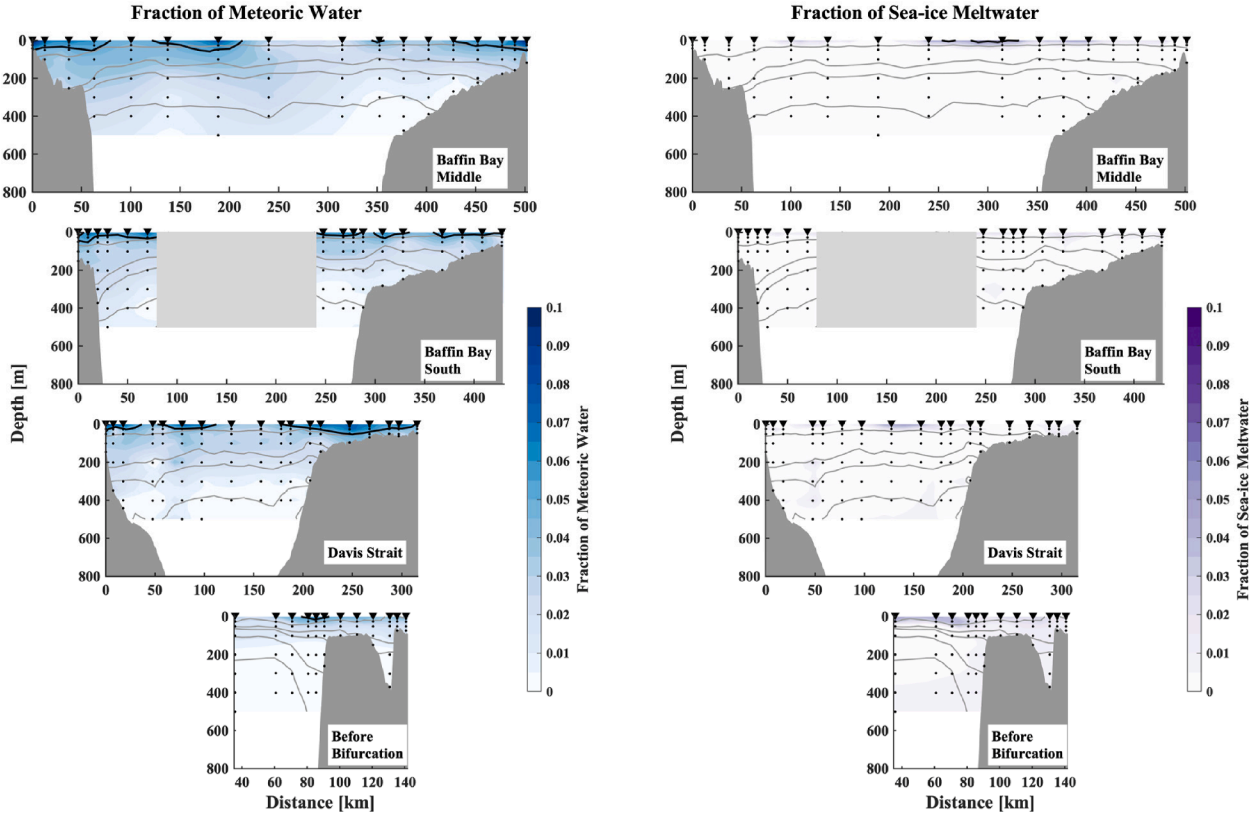

Fig. 9. Same as Fig. 8c except for the fraction of Meteoric Water (left) and Sea-Ice Meltwater (right). The value of 0.05 is indicated by the thick black contour. The data gap in the interior of Baffin Bay South section is masked in gray. Note that there were not enough $\delta^{18}O$ data collected on the After Bifurcation section to make such a plot, and the Baffin Bay North section consisted of XCTDs, hence no water sampling.

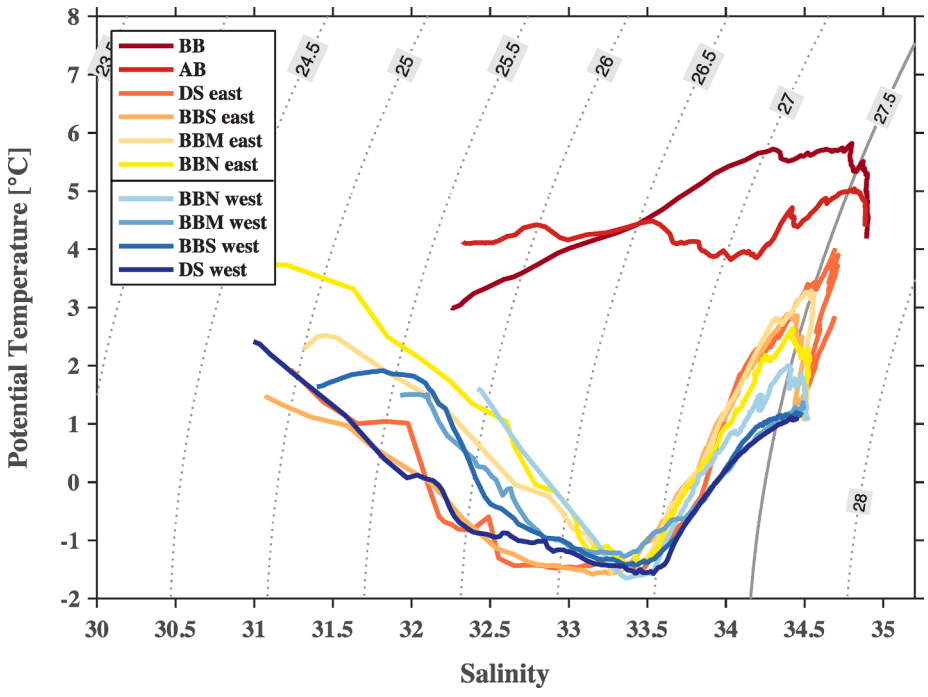

Fig. 10. Potential temperature-salinity diagram for the mean profiles in the eastern and western boundary current for each of the sections occupied during the *Healy* survey. The sections are indicated by different colors (see the legend): BB, Before Bifurcation; AB, After Bifurcation; DS, Davis Strait; BBS, Baffin Bay South; BBM, Baffin Bay Middle; BBN, Baffin Bay North. The dashed gray contours are potential density (kg/m^3), with the 27.5 kg/m^3 contour highlighted (solid line).

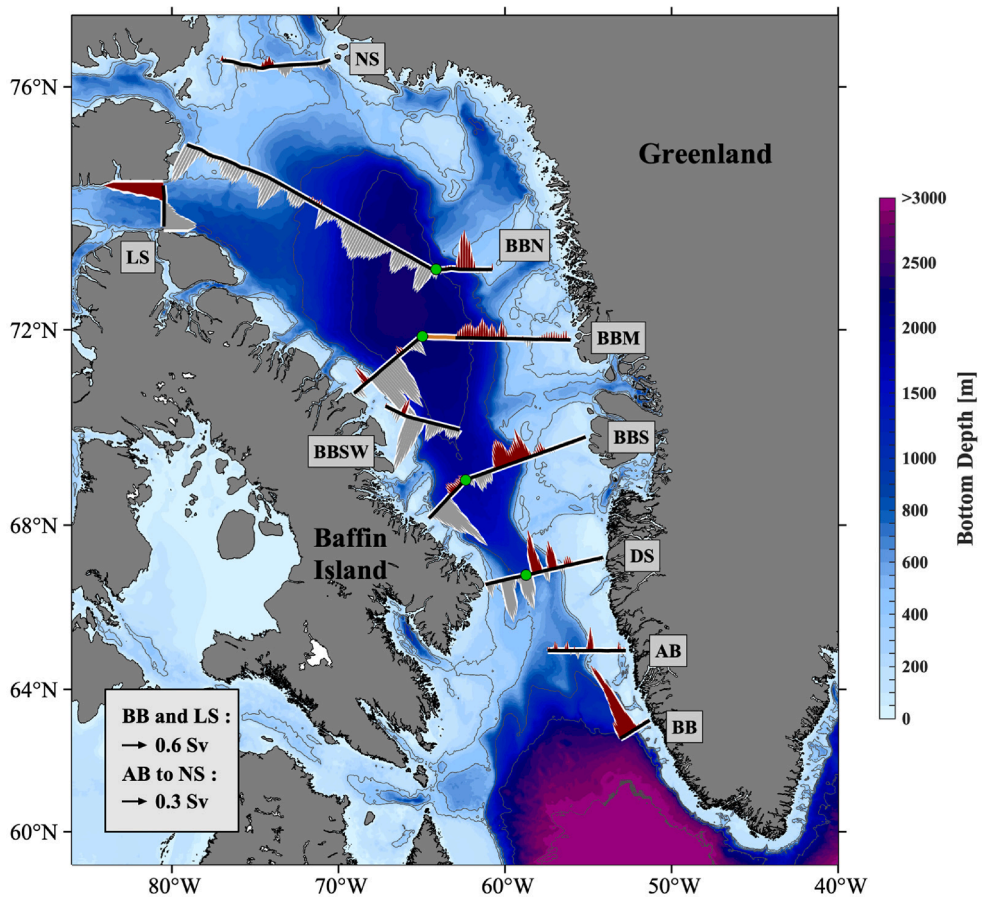

Fig. 11. Volume transport integrated over the upper 800 m of water column. The vectors show the magnitude of the transport (in Sv) per 5 km segment, with the northward (or westward for the LS section) and southward transport indicated by red and gray colors, respectively. Note the different scale for the BB and LS sections (see the legend). The bottom depth is from ETOPO1. The large anticyclonic eddy was excluded for the BBM section (the yellow segment). The green circle on each section indicates the division point between western and eastern Baffin Bay, which was used to compute the transports shown in Fig. 12.

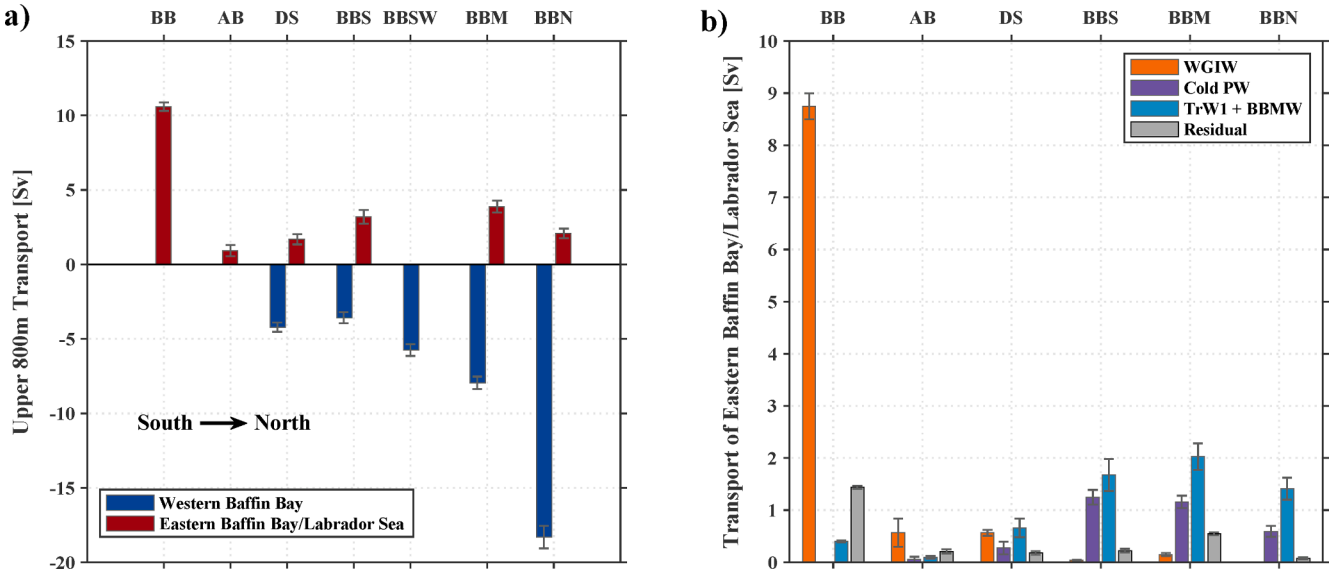

Fig. 12. (a) Upper 800 m transport of western Baffin Bay (blue) and eastern Baffin Bay/Labrador Sea (red) for each section occupied during the *Healy* survey. (b) Transport of the different dominant water masses in eastern Baffin Bay / Labrador Sea (WGIW, orange; cold PW, purple; TrW1 + BBMW, blue; and the residual water including warm PW, MWM and TrW2, gray). BBMW=Baffin Bay Mode Water.

To investigate the composition of the water contributing to the recirculation in southern/middle Baffin Bay, we separated the northward transport in the eastern bay by dominant water mass using the σ_0-π_0 distance approach (Fig. 12b). This reveals that the increase in northward transport from south to north is primarily associated with the cold PW and a combination of the deep TrW1 and BBMW. This confirms that some of the southward flowing cold PW along the western boundary current recirculates northward and joins the eastern boundary current. Such recirculation is also evident in the reanalysis dataset presented below, with low centers of geopotential height found in the interior of the Bay (Fig. 13b). Previous studies, using hydrographic data alone (Lobb et al., 2003; Myers & Ribergaard, 2013), have discussed the exchange of cold PW from the BIC into the WGC north of Davis Strait. Our velocity observations provide direct evidence of this.

3.5. *Variability of the basin-scale circulation and its relationship to wind forcing*

To shed more light on the basin-scale circulation in Baffin Bay, we use the ARMOR3D reanalysis product which provides 3-dimensional velocity and geopotential height data for each month from 1993 to 2021 (see Section 2.2). Fig. 13a,b compare the 50–300 m averaged ADCP velocity measured during the two shipboard surveys (29 August – 4 October 2021) to the 50–300 m averaged velocity from the reanalysis product for approximately the same time (September 2021). As with the direct velocity observations, the overall cyclonic circulation in Baffin Bay is evident in the reanalysis velocity field, with strong (weak) flow along the western (eastern) boundary and low geopotential height in the interior of the bay. Such agreement motivates us to use the reanalysis data to investigate the variability of the basin-scale circulation in Baffin Bay, which is helpful for understanding the representativeness of our velocity observations.

Comparing the September velocity field in 2021 with the September climatological mean velocity from 1993 to 2021 (Fig. 13b and 13c) reveals that the cyclonic circulation in Baffin Bay was much stronger for the year 2021 (see also the velocity anomalies in Fig. 13d). By contrast, the analogous calculation for September 2019 shows opposite anomalies for the interior circulation and geopotential height compared with the September climatological mean (September 2019 is an extreme opposite case over the last decade, see Supplementary Fig. 1). This indicates the large year-to-year variability of the basin-scale circulation in Baffin Bay.

Previous studies have pointed out the seasonality of the flows through the major gateways of Baffin Bay. For example, Curry et al. (2014) shows that the transport of northward-flowing WGIW through Davis Strait peaked in late fall to early winter. However, it remains unclear how this can be related to the seasonal variability of the basin-scale circulation in Baffin Bay. Although the ARMOR3D reanalysis provides monthly data throughout the year, this product is likely questionable in winter/early spring when the bay is fully covered by sea ice (note that the ARMOR3D data rely on the surface velocity derived from the satellite altimetry). Additional observational data covering different months of the year are required to better address the seasonality of the basin-scale circulation in Baffin Bay.

What are the driving mechanisms of the large circulation changes in September 2019 and 2021? To address this, we first investigate the impact of local wind forcing. In September 2021, a dipole-like wind stress curl pattern was present over the broad Baffin Bay region, with strong positive wind stress curl (WSC) in the northeastern bay and negative WSC near Davis Strait and the northern Labrador Sea (Fig. 14a). Such a dipole structure is also seen in the anomaly field when

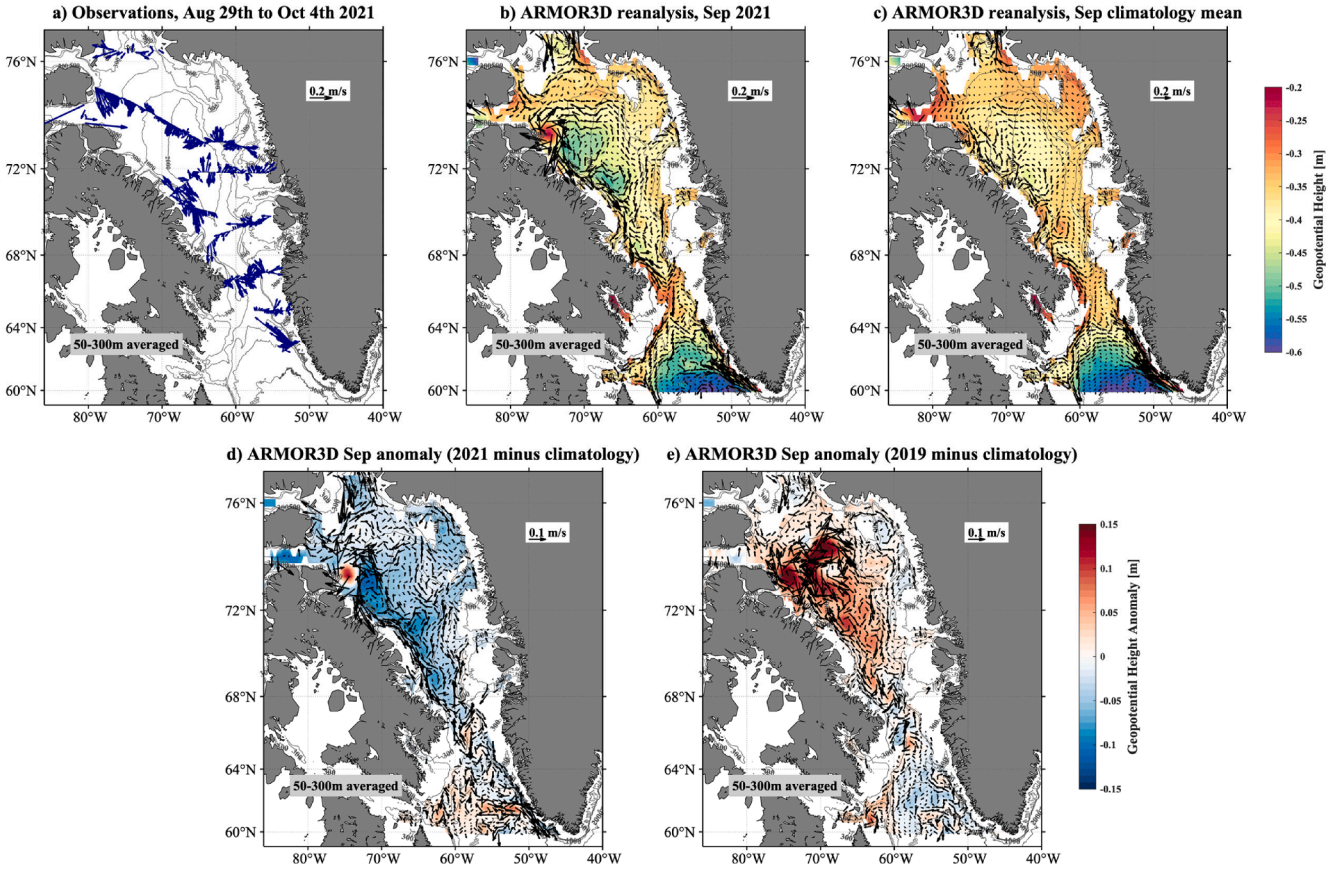

Fig. 13. (a) 50–300 m averaged ADCP velocity (vectors) from the two Baffin Bay surveys in 2021 (29 August – 4 October). (b) 50–300 m averaged velocity (vectors) and geopotential height (color) from the ARMOR3D reanalysis in September 2021. (c) Same as (b) for the September climatological mean from 1993 to 2021. (d) Anomalies of (b) compared with (c). (e) Same as (d) for 2019. The bathymetry (gray contours) is from ETOPO1.

subtracting the climatological mean (Fig. 14b). The resulting drop in sea surface height (SSH) in Baffin Bay enhances the cyclonic circulation and leads to more eastward recirculation of the western boundary current in the southern bay (note that the anomalous northernly wind south of Davis Strait can weaken the WGC and reduce the amount of the WGIW penetration into Baffin Bay). A similar relationship between positive WSC and enhanced cyclonic circulation is found throughout the full ARMOR3D time period (1993–2021) during the warm months of the year (July-October). This suggests that such local wind forcing contributed to the strong cyclonic circulation observed during the 2021 shipboard surveys. However, a different pattern of WSC anomaly occurred for September 2019 (Fig. 14c), which is not able to explain the existence of the anticyclone-like velocity anomalies for that month (Fig. 13e). This implies that there was an additional mechanism(s) impacting the basin-scale circulation in the bay for that time period.

Previous studies based on observations and numerical models (Peterson et al., 2012; Grivault et al., 2018; Myers et al., 2021) have discussed the role of remote winds on the circulation of the Canadian Arctic Archipelago. For example, using a multi-year mooring dataset Peterson et al. (2012) demonstrated that cyclonic wind forcing over the western Arctic can enhance the volume transport through Lancaster Sound. To investigate the role of remote atmospheric forcing on the basin-scale circulation in Baffin Bay, we compared the July to September mean sea level pressure and wind anomaly in 2021 and 2019 (relative to the July to September climatological mean from 1993 to 2021) over the entire Arctic domain. We note that the cyclonic and anticyclonic circulation anomalies in Baffin Bay present in September 2021 and 2019, respectively, also existed in July and August of those years. Interestingly, in 2021 there was a broad-scale negative sea level pressure and cyclonic wind anomaly in the western Arctic (Fig. 15a). This corresponded to a positive phase of Arctic Oscillation (AO). By contrast, in 2019 there was a strong positive sea level pressure and anticyclonic wind anomaly, which corresponded to a negative phase of the AO. In the numerical modeling study of Wang & Danilov (2022), a positive AO anomaly was linked with a lower SSH in Baffin Bay and enhanced cyclonic basin-scale circulation (see their Fig. 4). One possible explanation for such a link is that the increase in SSH along the southern edge of the Canada Basin (i.e., along the edge of the Canadian Arctic Archipelago) due to the cyclonic wind anomaly (positive AO) can propagate into Baffin Bay through the archipelago, which increases the onshore-offshore SSH gradient and in turn generates cyclone-like circulation anomalies in the bay. Additional work is required to systematically address the impact of wind forcing on the basin-scale circulation of Baffin Bay, including the relative importance of local versus remote wind forcing, which is beyond the scope of this study. Future observational and modeling studies are required to address this.

4. Summary

In this study, hydrographic, nutrient, oxygen isotope, and velocity data collected from two surveys in late-summer to early-fall 2021 were used to advance our understanding of the water mass evolution and general circulation in Baffin Bay. Four dominant water masses were identified and mapped using high-resolution CTD data and the potential density-potential spicity (σ_0-π_0) distance methodology: the warm and salty Atlantic-origin West Greenland Irminger Water (WGIW); the cold and relatively fresh Polar Water (cold PW); the warm and fresh Polar Water (warm PW); and a combination of very fresh sea-ice meltwater and meteoric water (MWM). The two types of PW were prevalent in the upper 300 m of Baffin Bay, with the coldest and freshest, nitrate-depleted PW dominant along the western shelf and slope. Only a small amount of WGIW was measured entering the southeastern bay at depth. This water mass, with relatively low phosphate and silicate content, is diluted rapidly when crossing Davis Strait and is then transformed more gradually as it flows northward along the Greenland continental slope due to the mixing with the cold and fresh PW. The MWM was found to occupy the surface layer over most of Baffin Bay, except for the West Greenland shelf where the warm PW was more dominant. Since the characterization of water masses based on the nutrient distributions agree well with the hydrographic data, we mainly used the chemical data to investigate more specifically the sources of PW and freshwater composition. Although the spatial resolution of nutrient and oxygen isotope data is much coarser than that of the CTD data, our results indicate that the upper 200 m in western Baffin Bay contains high fractions of Pacific-origin water (>0.5). By contrast, the fractions of meteoric water and sea-ice meltwater are much lower (<0.1) throughout Baffin Bay, with the latter lower than 0.02. Relatively high fractions of meteoric water occurred at the surface on both sides of the bay.

The circulation during late-summer to early-fall 2021 in Baffin Bay was cyclonic, consisting of a strong, surface-intensified western boundary current and a slower, weakly baroclinic eastern boundary

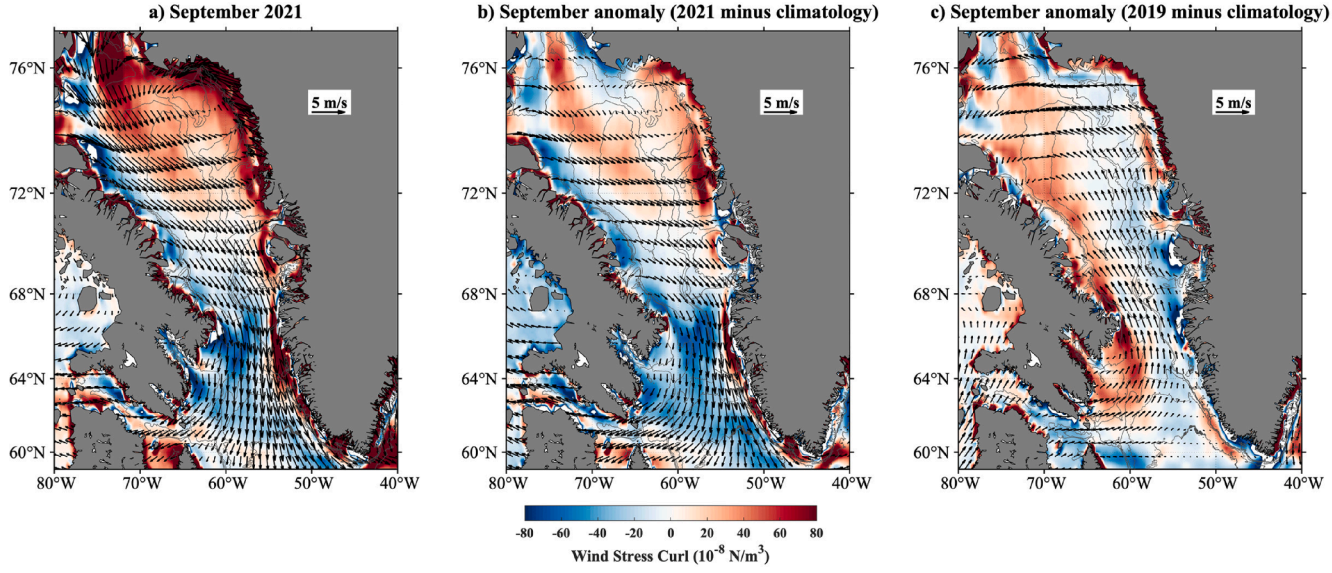

Fig. 14. (a) 10-m wind (vectors) and wind stress curl (color) in September 2021. (b) anomalies of (a) relative to the September climatological mean from 1993 to 2021. (c) Same as (b) for 2019. The data are from ERA5.

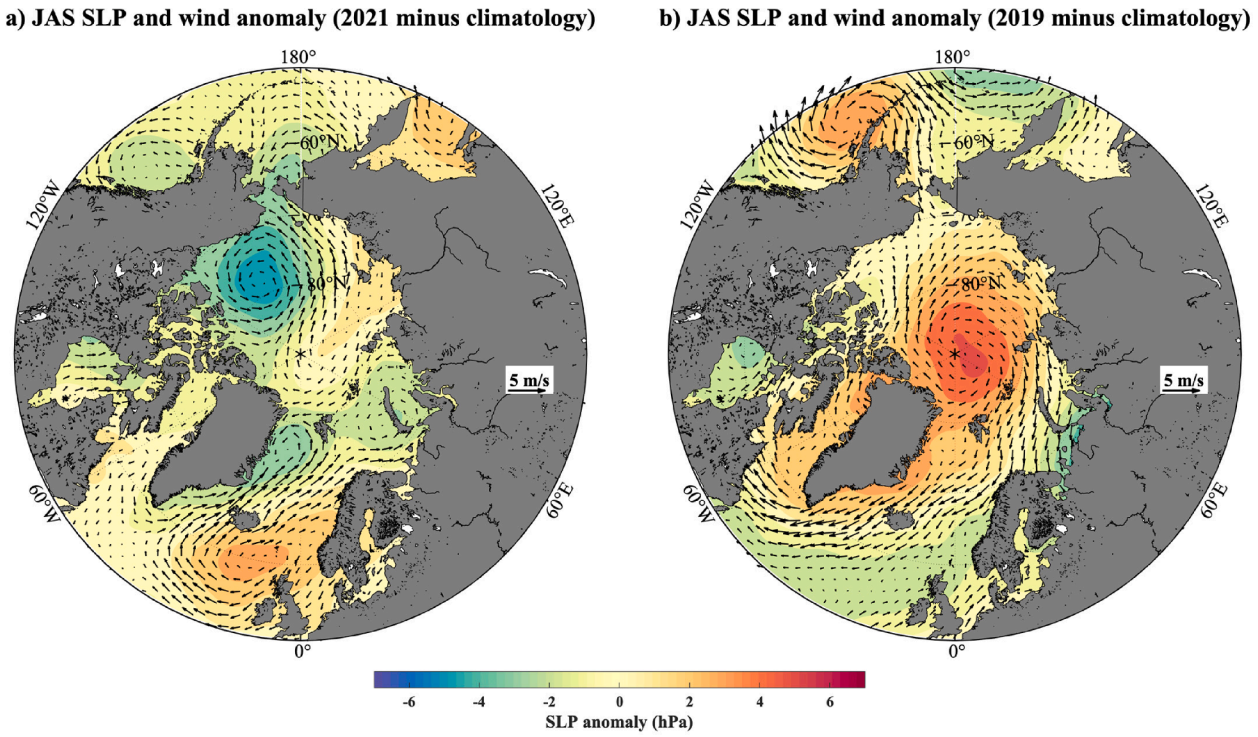

Fig. 15. Anomalies of sea level pressure (color) and wind (vectors) for July-September 2021 (left) and 2019 (right) compared with the July-September climatological mean from 1993 to 2021. The data are from ERA5.

current. There were significant changes in the structure of eastern boundary current as it progressed northward. Much of the current bifurcated to the west at the northern end of the Labrador Sea, and, as the remaining flow progressed through Davis Strait, it transitioned from surface-intensified to bottom-intensified. An anticyclonic eddy similar to a Labrador Sea Irminger Ring was observed in the interior of Baffin Bay, indicating that such slope-basin exchange occurs farther north along the West Greenland Current. A north-to-south reduction of southward transport was found along the western Baffin Bay continental slope, concomitant with increased northward transport along the eastern Baffin Bay continental slope. These trends, together with the observed double core structure of the boundary current on both sides of the bay, suggests that recirculation in southern Baffin Bay transports some of the cold PW from the western boundary to the eastern boundary.

The consistency between the directly measured velocity from the *Healy* survey and the 3-dimentional velocity field from the ARMOR3D ocean reanalysis product motivated further investigation of the variability of the basin-scale circulation in Baffin Bay. It was found that there was a cyclonic (anticyclonic) basin-scale circulation anomaly for September 2021 (2019) compared with the September climatological mean. Using atmospheric reanalysis data, it appears that both the local wind stress curl pattern and remote wind forcing associated with the AO index can lead to such Baffin Bay circulation anomalies, although additional work is required to address these two driving mechanisms in more detail. As the climate continues to warm, more observational data will be needed to better understand the seasonal to long-term variability of the circulation and water mass distribution throughout Baffin Bay. This is imperative for determining the fate of the freshwater exiting the Arctic Ocean, as well as the role of subtropical-origin heat on the retreat of Greenland's glaciers.

CRediT authorship contribution statement

Jie Huang: Writing – review & editing, Writing – original draft, Visualization, Methodology, Investigation, Formal analysis, Data curation, Conceptualization. **Robert S. Pickart:** Writing – review & editing, Writing – original draft, Supervision, Resources, Methodology, Investigation, Funding acquisition, Data curation, Conceptualization. **Frank Bahr:** Writing – review & editing, Validation, Methodology, Data curation. **Leah T. McRaven:** Writing – review & editing, Validation, Methodology, Data curation. **Jean-Éric Tremblay:** Writing – review & editing, Resources, Funding acquisition, Data curation. **Christine Michel:** Writing – review & editing, Resources, Funding acquisition, Data curation. **Emil Jeansson:** Writing – review & editing, Resources, Funding acquisition, Data curation. **Ben Kopec:** Writing – review & editing, Resources, Methodology, Data curation. **Jeffrey M. Welker:** Writing – review & editing, Resources, Funding acquisition, Data curation. **Sólveig R. Ólafsdóttir:** Writing – review & editing, Methodology, Data curation.

Declaration of competing interest

The authors declare that they have no known competing financial interests or personal relationships that could have appeared to influence the work reported in this paper.

Data availability

The data from the *Healy* survey in 2021 are available at DOI: https://arcticdata.io/catalog/view/doi:10.18739/A2DB7VR5M.

The data from the *Amundsen* survey in 2021 are available at DOI: https://doi.org/10.5884/12713.

The ERA5 wind and sea level pressure data are available at: https://www.ecmwf.int/en/forecasts/datasets/reanalysis-datasets/era5. DOI: https://doi.org/10.1002/qj.3803.

The velocity and geopotential height data from ARMORD reanalysis are available at https://data.marine.copernicus.eu/product/MULTIOBS_GLO_PHY_TSUV_3D_MYNRT_015_012. https://doi.org/10.48670/moi-00052.

Acknowledgements

The authors are indebted to the crews of the USCGC *Healy* and CCGS *Amundsen* for their hard work and dedication in carrying out the shipboard measurements. The authors thank Daniel Torres for de-tiding the *Amundsen* velocity data, and Valtteri Hyöky, Tarja Törmänen, Aino Erkinaro, and Kaisa-Riikka Mustonen for assisting with the isotopic sample processing. Funding was provided by the U. S. National Science Foundation under grant OPP-2211691 (Jie Huang and Robert Pickart) and OPP-2133156 (Jeffrey Welker and Ben Kopec); Canada ArcticNet Network of Centers of Excellence Grant P19 - Nutrient Transports and Living Marine Resources across the Inuit Nunangat (Jean-Éric Tremblay); the Bjerknes Centre for Climate Research (Emil Jeansson); and the University of Oulu, Arctic Interaction, High Risk-High Reward award (Jeffrey Welker). Additional support from Jeffrey Welker's UArctic Research Chairmanship was instrumental in the success of this research.

Appendix A. Supplementary material

Supplementary data to this article can be found online at https://doi.org/10.1016/j.pocean.2024.103322.

References

Alkire, M.B., Rember, R., Polyakov, I., 2019. Discrepancy in the identification of the Atlantic/Pacific front in the central Arctic Ocean: NO versus nutrient relationships. Geophys. Res. Lett. 46, 3843–3852.

Amundsen Science Data Collection. 2021. CTD data collected by the CCGS Amundsen in the Canadian Arctic. ArcticNet Inc., Québec, Canada. Processed data. Version 1. Archived at www.polardata.ca, Canadian Cryospheric Information Network (CCIN), Waterloo, Canada. https://doi.org/10.5884/12713.

Amundsen Science Data Collection. 2021. LADCP data collected by the CCGS Amundsen in the Canadian Arctic. ArcticNet.Inc., Quebec, Canada. Processed data. Version 1. Archived at www.polardata.ca, Canadian Cryospheric Information Network (CCIN)., Waterloo, Canada. doi: 10.5884/12714.

Azetsu-Scott, K., Clarke, A., Falkner, K., Hamilton, J., Jones, E.P., Lee, C., Petrie, B., Prinsenberg, S., Starr, M., Yeats, P., 2010. Calcium carbonate saturation states in the waters of the Canadian Arctic Archipelago and the Labrador Sea. J. Geophys. Res. Oceans 115, C11021.

Azetsu-Scott, K., Petrie, B., Yeats, P., Lee, C., 2012. Composition and fluxes of freshwater through Davis Strait using multiple chemical tracers. J. Geophys. Res. Oceans 117, C12011.

Bashmachnikov, I.L., Fedorov, A.M., Golubkin, P.A., Vesman, A.V., Selyuzhenok, V.V., Gnatiuk, N.V., Bobylev, L.P., Hodges, K.I., Dukhovskoy, D.S., 2021. Mechanisms of interannual variability of deep convection in the Greenland sea. Deep Sea Res. Part I 174, 103557.

Böning, C.W., Behrens, E., Biastoch, A., Getzlaff, K., Bamber, J.L., 2016. Emerging impact of Greenland meltwater on deepwater formation in the North Atlantic Ocean. Nat. Geosci. 9, 523–527.

Bracco, A., Pedlosky, J., Pickart, R.S., 2008. Eddy formation near the west coast of Greenland. J. Phys. Oceanogr. 38, 1992–2002.

Buckley, M.W. and Marshall, J., 2016. Observations, inferences, and mechanisms of the Atlantic Meridional Overturning Circulation: A review. *Reviews of Geophysics*, *54*(1), pp.5-63.

Carroll, D., Sutherland, D., Curry, B., Nash, J., Shroyer, E., Catania, G., Stearns, L., Grist, J., Lee, C., de Steur, L., 2018. Subannual and seasonal variability of Atlantic-origin waters in two adjacent west Greenland fjords. J. Geophys. Res. Oceans 123, 6670–6687.

Cuny, J., Rhines, P.B., Niiler, P.P., Bacon, S., 2002. Labrador Sea boundary currents and the fate of the Irminger Sea Water. J. Phys. Oceanogr. 32, 627–647.

Curry, B., Lee, C., Petrie, B., Moritz, R., Kwok, R., 2014. Multiyear volume, liquid freshwater, and sea ice transports through Davis Strait, 2004–10. J. Phys. Oceanogr. 44, 1244–1266.

De Jong, M., Bower, A., Furey, H., 2014. Two years of observations of warm-core anticyclones in the Labrador Sea and their seasonal cycle in heat and salt stratification. J. Phys. Oceanogr. 44, 427–444.

Dodd, P.A., Rabe, B., Hansen, E., Falck, E., Mackensen, A., Rohling, E., Stedmon, C., Kristiansen, S., 2012. The freshwater composition of the Fram Strait outflow derived from a decade of tracer measurements. J. Geophys. Res. Oceans 117, C11005.

Dukhovskoy, D.S., Myers, P.G., Platov, G., Timmermans, M.L., Curry, B., Proshutinsky, A., Bamber, J.L., Chassignet, E., Hu, X., Lee, C.M., 2016. Greenland freshwater pathways in the sub-A rctic S eas from model experiments with passive tracers. J. Geophys. Res. Oceans 121, 877–907.

Dunlap, E., Tang, C.C., 2006. Modelling the mean circulation of Baffin Bay. Atmos. Ocean 44, 99–109.

Ekwurzel, B., Schlosser, P., Mortlock, R.A., Fairbanks, R.G., Swift, J.H., 2001. River runoff, sea ice meltwater, and Pacific water distribution and mean residence times in the Arctic Ocean. J. Geophys. Res. Oceans 106, 9075–9092.

Firing E., and Hummon J.M., 2010. The GO-SHIP Repeat Hydrographic Manual: A Collection of Expert Reports and Guidelines. IOCCP Report No 14.

Firing, E., Hummon, J.M., Chereskin, T.K., 2012. Improving the quality and accessibility of current profile measurements in the Southern Ocean. Oceanography 25 (3), 164–165.

Foukal, N.P., Pickart, R.S., 2023. Moored observations of the West Greenland Coastal current along the Southwest Greenland Shelf. J. Phys. Oceanogr. 53, 2619–2632.

Gelderloos, R., Katsman, C.A., Drijfhout, S.S., 2011. Assessing the roles of three eddy types in restratifying the Labrador Sea after deep convection. J. Phys. Oceanogr. 41, 2102–2119.

Gladish, C.V., Holland, D.M. and Lee, C.M., 2015. Oceanic boundary conditions for Jakobshavn Glacier. Part II: Provenance and sources of variability of Disko Bay and Ilulissat icefjord waters, 1990–2011. *Journal of Physical Oceanography*, *45*(1), pp.33-63.

Gou, R., Pennelly, C., Myers, P.G., 2022. The changing behavior of the West Greenland current system in a very high-resolution model. J. Geophys. Res. Oceans 127 (8), e2022JC018404.

Grivault, N., Hu, X., Myers, P.G., 2018. Impact of the surface stress on the volume and freshwater transport through the Canadian Arctic Archipelago from a high-resolution numerical simulation. J. Geophys. Res. Oceans 123, 9038–9060.

Guinehut, S., Dhomps, A.L., Larnicol, G., Le Traon, P.Y., 2012. High resolution 3-D temperature and salinity fields derived from in situ and satellite observations. Ocean Sci. 8 (5), 845–857.

Håvik, L., Pickart, R., Våge, K., Torres, D., Thurnherr, A., Beszczynska-Möller, A., Walczowski, W., von Appen, W.J., 2017. Evolution of the E ast G reenland C urrent from F ram S trait to D enmark S trait: Synoptic measurements from summer 2012. J. Geophys. Res. Oceans 122, 1974–1994.

Hersbach, H., Bell, B., Berrisford, P., Hirahara, S., Horányi, A., Muñoz-Sabater, J., Nicolas, J., Peubey, C., Radu, R., Schepers, D., Simmons, A., 2020. The ERA5 global reanalysis. Q. J. R. Meteorolog. Soc. 146 (730), 1999–2049.

Holland, D.M., Thomas, R.H., De Young, B., Ribergaard, M.H., Lyberth, B., 2008. Acceleration of Jakobshavn Isbræ triggered by warm subsurface ocean waters. Nat. Geosci. 1, 659–664.

Huang, J., Pickart, R.S., Huang, R.X., Lin, P., Brakstad, A., Xu, F., 2020. Sources and upstream pathways of the densest overflow water in the Nordic Seas. Nat. Commun. 11, 5389.

Huang, J., Pickart, R.S., Bahr, F., McRaven, L.T., Xu, F., 2021. Wintertime water mass transformation in the western Iceland and Greenland Seas. J. Geophys. Res. Oceans 126, e2020JC016893.

Huang, J., Pickart, R.S., Foukal, N., Spall, M.A., Lin, P., 2023a. Structure and variability of the Barrow Canyon outflow from two high-resolution shipboard surveys in 2018. J. Geophys. Res. Oceans, e2023JC019640.

Huang, J., Pickart, R.S., Chen, Z., Huang, R.X., 2023b. Role of air-sea heat flux on the transformation of Atlantic Water encircling the Nordic Seas. Nat. Commun. 14, 141.

Huang, R.X., Yu, L.S., Zhou, S.Q., 2018. New definition of potential spicity by the least square method. J. Geophys. Res. Oceans 123, 7351–7365.

Jones, E.P., Anderson, L.G., Swift, J.H., 1998. Distribution of Atlantic and Pacific waters in the upper Arctic Ocean: Implications for circulation. Geophys. Res. Lett. 25, 765–768.

Jones, E.P., Anderson, L.G., Jutterström, S., Mintrop, L., Swift, J.H., 2008. Pacific freshwater, river water and sea ice meltwater across Arctic Ocean basins: Results from the 2005 Beringia Expedition. J. Geophys. Res. Oceans 113.

Jones, E., Swift, J., Anderson, L., Lipizer, M., Civitarese, G., Falkner, K., Kattner, G., McLaughlin, F., 2003. Tracing Pacific water in the North Atlantic ocean. J. Geophys. Res. Oceans 108.

Katsman, C.A., Spall, M.A., Pickart, R.S., 2004. Boundary current eddies and their role in the restratification of the Labrador Sea. J. Phys. Oceanogr. 34, 1967–1983.

Lazier, J.R., 1980. Oceanographic conditions at ocean weather ship Bravo, 1964–1974. Atmos. Ocean 18, 227–238.

Lilly, J.M., Rhines, P.B., Schott, F., Lavender, K., Lazier, J., Send, U., D'Asaro, E., 2003. Observations of the Labrador Sea eddy field. Prog. Oceanogr. 59, 75–176.

Lin, P., Pickart, R.S., Torres, D.J., Pacini, A., 2018. Evolution of the freshwater coastal current at the southern tip of Greenland. J. Phys. Oceanogr. 48, 2127–2140.

Lin, P., Pickart, R.S., Heorton, H., Tsamados, M., Itoh, M., Kikuchi, T., 2023. Recent state transition of the Arctic Ocean's Beaufort Gyre. Nat. Geosci. 1–7.

Lobb, J., Carmack, E.C., Ingram, R.G., Weaver, A.J., 2003. Structure and mixing across an Arctic/Atlantic front in northern Baffin Bay. Geophys. Res. Lett. 30 (16), 1833.

McRaven, L., 2022. Shipboard hydrographic measurements from the Fate of freshwater and heat from the West Greenland Current project (2021). Arctic Data Center. https://doi.org/10.18739/A2DB7VR5M.

Melling, H., Agnew, T.A., Falkner, K.K., Greenberg, D.A., Lee, C.M., Münchow, A., Petrie, B., Prinsenberg, S.J., Samelson, R.M., Woodgate, R.A., 2008. Fresh-water fluxes via Pacific and Arctic outflows across the Canadian polar shelf. *Arctic–Subarctic Ocean Fluxes: Defining the Role of the Northern Seas in Climate*, 193-247.

Melling, H., Gratton, Y., Ingram, G., 2001. Ocean circulation within the North Water polynya of Baffin Bay. Atmos. Ocean 39 (3), 301–325.

Mortensen, J., Rysgaard, S., Arendt, K., Juul-Pedersen, T., Søgaard, D., Bendtsen, J., Meire, L., 2018. Local coastal water masses control heat levels in a West Greenland tidewater outlet glacier fjord. J. Geophys. Res. Oceans 123, 8068–8083.

Mortensen, J., Rysgaard, S., Winding, M.H.S., Juul-Pedersen, T., Arendt, K.E., Lund, H., Stuart-Lee, A.E., Meire, L., 2022. Multidecadal water mass dynamics on the West Greenland Shelf. J. Geophys. Res. Oceans 127 (7), e2022JC018724.

Mulet, S., Rio, M.H., Mignot, A., Guinehut, S., Morrow, R., 2012. A new estimate of the global 3D geostrophic ocean circulation based on satellite data and in-situ measurements. Deep Sea Res. Part II 77, 70–81.

Münchow, A., 2016. Volume and freshwater flux observations from Nares Strait to the west of Greenland at daily time scales from 2003 to 2009. J. Phys. Oceanogr. 46, 141–157.
Münchow, A., Falkner, K.K., Melling, H., 2015. Baffin island and west Greenland current systems in northern Baffin bay. Prog. Oceanogr. 132, 305–317.
Myers, P.G., Ribergaard, M.H., 2013. Warming of the polar water layer in Disko Bay and potential impact on Jakobshavn Isbrae. J. Phys. Oceanogr. 43 (12), 2629–2640.
Myers, P.G., Castro de la Guardia, L., Fu, C., Gillard, L.C., Grivault, N., Hu, X., Lee, C.M., Moore, G., Pennelly, C., Ribergaard, M.H., 2021. Extreme high Greenland Blocking Index leads to the reversal of Davis and Nares Strait net transport toward the Arctic Ocean. Geophys. Res. Lett. 48, e2021GL094178.
Pacini, A., Pickart, R.S., 2022. Meanders of the west Greenland current near cape farewell. Deep Sea Res. Part I 179, 103664.
Pacini, A., Pickart, R.S., Bahr, F., Torres, D.J., Ramsey, A.L., Holte, J., Karstensen, J., Oltmanns, M., Straneo, F., Le Bras, I.A., 2020. Mean conditions and seasonality of the west Greenland boundary current system near cape farewell. J. Phys. Oceanogr. 50, 2849–2871.
Peterson, I., Hamilton, J., Prinsenberg, S., Pettipas, R., 2012. Wind-forcing of volume transport through Lancaster Sound. J. Geophys. Res. Oceans 117.
Pickart, R.S., Lin, P., Bahr, F., McRaven, L.T., Huang, J., Pacini, A., Arrigo, K.R., Ashjian, C.J., Berchok, C., Baumgartner, M.F., 2023. The Pacific Water flow branches in the eastern Chukchi Sea. Prog. Oceanogr., 103169
Pickart, R.S., Smethie, W.M., 1998. Temporal evolution of the deep western boundary current where it enters the sub-tropical domain. Deep Sea Res. Part I 45, 1053–1083.
Proshutinsky, A., Krishfield, R., Timmermans, M.L., Toole, J., Carmack, E., McLaughlin, F., Williams, W.J., Zimmermann, S., Itoh, M., Shimada, K., 2009. Beaufort Gyre freshwater reservoir: State and variability from observations. J. Geophys. Res. Oceans 114.
Rabe, B., Johnson, H.L., Münchow, A., Melling, H., 2012. Geostrophic ocean currents and freshwater fluxes across the Canadian polar shelf via Nares Strait. J. Mar. Res. 70 (4), 603–640.
Renfrew, I.A., Barrell, C., Elvidge, A., Brooke, J., Duscha, C., King, J., Kristiansen, J., Cope, T.L., Moore, G.W.K., Pickart, R.S., 2021. An evaluation of surface meteorology and fluxes over the Iceland and Greenland Seas in ERA5 reanalysis: The impact of sea ice distribution. *Quarterly Journal of the Royal Meteorological Society*, 147, 691-712.
Rossby, T., 1996. The North Atlantic Current and surrounding waters: At the crossroads. Reviews of Geophysics 34 (4), 463–481.
Rysgaard, S., Boone, W., Carlson, D., Sejr, M.K., Bendtsen, J., Juul-Pedersen, T., Lund, H., Meire, L., Mortensen, J., 2020. An updated view on water masses on the pan-west Greenland continental shelf and their link to proglacial fjords. J. Geophys. Res. Oceans 125 (2), e2019JC015564.
Solomon, A., Heuzé, C., Rabe, B., Bacon, S., Bertino, L., Heimbach, P., Inoue, J., Iovino, D., Mottram, R., Zhang, X., 2021. Freshwater in the arctic ocean 2010–2019. Ocean Sci. 17, 1081–1102.
Straneo, F., Sutherland, D.A., Holland, D., Gladish, C., Hamilton, G.S., Johnson, H.L., Rignot, E., Xu, Y., Koppes, M., 2012. Characteristics of ocean waters reaching Greenland's glaciers. Ann. Glaciol. 53, 202–210.
Sutherland, D.A., Pickart, R.S., Peter Jones, E., Azetsu-Scott, K., Jane Eert, A., Ólafsson, J., 2009. Freshwater composition of the waters off southeast Greenland and their link to the Arctic Ocean. J. Geophys. Res. Oceans 114.
Tang, C.C., Ross, C.K., Yao, T., Petrie, B., DeTracey, B.M., Dunlap, E., 2004. The circulation, water masses and sea-ice of Baffin Bay. Prog. Oceanogr. 63, 183–228.
Tremblay, J.É., Anderson, L.G., Matrai, P., Coupel, P., Bélanger, S., Michel, C., Reigstad, M., 2015. Global and regional drivers of nutrient supply, primary production and CO2 drawdown in the changing Arctic Ocean. Prog. Oceanogr. 139, 171–196.
Wang, Q., Danilov, S., 2022. A synthesis of the upper Arctic Ocean circulation during 2000–2019: Understanding the roles of wind forcing and sea ice decline. Front. Mar. Sci. 9, 863204.
Wang, Q., Myers, P.G., Hu, X., Bush, A.B., 2012. Flow constraints on pathways through the Canadian Arctic Archipelago. Atmos. Ocean 50 (3), 373–385.
Wang, Q., Shu, Q., Danilov, S., Sidorenko, D., 2022. An extreme event of enhanced Arctic Ocean export west of Greenland caused by the pronounced dynamic sea level drop in the North Atlantic subpolar gyre in the mid-to-late 2010s. Environ. Res. Lett. 17, 044046.
Yamamoto-Kawai, M., McLaughlin, F., Carmack, E., Nishino, S., Shimada, K., 2008. Freshwater budget of the Canada Basin, Arctic Ocean, from salinity, δ18O, and nutrients. J. Geophys. Res. Oceans 113.
Zhang, Y., Chen, C., Beardsley, R.C., Gao, G., Lai, Z., Curry, B., Lee, C.M., Lin, H., Qi, J., Xu, Q., 2016. Studies of the Canadian Arctic Archipelago water transport and its relationship to basin-local forcings: Results from AO-FVCOM. J. Geophys. Res. Oceans 121, 4392–4415.
Zhang, J., Weijer, W., Steele, M., Cheng, W., Verma, T., Veneziani, M., 2021. Labrador Sea freshening linked to Beaufort Gyre freshwater release. Nat. Commun. 12, 1229.
Zweng, M.M., Münchow, A., 2006. Warming and freshening of Baffin Bay, 1916–2003. J. Geophys. Res. Oceans 111.